

Arctic Mixed-phase Clouds Simulated by a Cloud-Resolving Model: Comparison with ARM Observations and Sensitivity to Microphysics Parameterizations

Yali Luo^{1,2}, Kuan-Man Xu²,
Hugh Morrison³, Greg McFarquhar⁴

¹ National Institute of Aerospace, Hampton, VA

² NASA Langley Research Center, Hampton, VA

³ National Center for Atmospheric Research, Boulder, CO

⁴ University of Illinois at Urbana-Champaign, Urbana, IL

March 15, 2007

Submitted to *J. Atmos. Sci.*

Corresponding author:

Dr. Yali Luo

MS 420, NASA Langley Research Center, Hampton, VA 23681.

Email: y.luo@larc.nasa.gov

ABSTRACT

Single-layer mixed-phase stratiform (MPS) Arctic clouds, which formed under conditions of large surface heat flux combined with general subsidence during a subperiod of the Atmospheric Radiation Measurement (ARM) Program Mixed-Phase Arctic Cloud Experiment (M-PACE), are simulated with a cloud resolving model (CRM). The CRM is implemented with either an advanced two-moment (M05) or a commonly used one-moment (L83) bulk microphysics scheme and a state-of-the-art radiative transfer scheme.

The CONTROL simulation, that uses the M05 scheme and observed aerosol size distribution and ice nuclei (IN) number concentration, reproduces the magnitudes and vertical structures of cloud liquid water content (LWC), total ice water content (IWC), number concentration and effective radius of cloud droplets as suggested by the M-PACE observations. It underestimates ice crystal number concentrations by an order of magnitude and overestimates effective radius of ice crystals by a factor of 2-3. The OneM experiment, that uses the L83 scheme, produces values of liquid water path (LWP) and ice plus snow water path (ISWP) that were about 30% and 4 times, respectively, of those produced by the CONTROL. Its vertical profile of IWC exhibits a bimodal distribution in contrast to the constant distribution of IWC produced in the CONTROL and observations.

A sensitivity test that uses the same ice-water saturation adjustment scheme as in OneM produces cloud properties that are more similar to the OneM than the CONTROL. The CONTROL predicts spatially varying values of the intercept parameter of snow size spectra (N_{0s}) that are one order of magnitude smaller than the prescribed N_{0s} used in L83. A sensitivity test that prescribes the larger L83 N_{0s} results in 20% less LWP and 5 times larger snow water path than the CONTROL. When an exponential ice size distribution replaces the gamma size distribution in the CONTROL, ISWP decreases by 70% but LWP increases by 7% versus the CONTROL. Increasing the IN number concentration from the observed value of $0.16 L^{-1}$ to $3.2 L^{-1}$ forces the MPS clouds to become glaciated and dissipate, but the simulated ice number concentration agrees initially with the observations better. Physical explanations for these quantitative differences are

provided. It is further shown that the differences between the OneM and the CONTROL are larger than those due to the estimated uncertainties in the prescribed surface fluxes. Additional observations and simulations of a variety of cases is required to further narrow down uncertainties in the microphysics schemes.

1. Introduction

Atmospheric numerical models with a horizontal grid spacing of 1 - 2 km are known as cloud-resolving models (CRMs). CRMs are able to resolve convective-scale and mesoscale circulations and, hence, can better represent the interactions between physical processes involving smaller scales than traditional General Circulation Models (GCMs). Physical processes such as those involving clouds and precipitation cannot be explicitly resolved and have to be parameterized in GCMs because of the grid spacing of a GCM, which is typically on the order of 100 km in the horizontal and 1 km in the vertical. Unfortunately, there are large uncertainties in parameterizations of subgrid scale processes and improvement of parameterizations has been slow in spite of the enormous efforts made over the past decades (Randall et al. 2003). Moreover, the subgrid-scale processes interact mainly through the time-varying large-scale variables (and surface conditions) in GCMs while in reality they directly interact with each other. A unified formulation of the entire spectrum of these interactions is necessary for more accurate climate and weather prediction, but it is difficult to achieve this with the traditional grid spacings used in GCMs (Arakawa 2004). Therefore, with the rapid growth of computational capacity, continental-scale NWP is currently performed at cloud-resolving scales (e.g. WRF; Skamarock et al. 2005). For climate simulation, CRMs have been used as a “super-parameterization” to replace most of the traditional parameterizations in each grid cell of GCMs (e.g. Grabowski 2003) and global versions of CRMs are emerging (Tomita et al. 2005).

Microphysical processes, as well as turbulent and radiative transfer processes, still need to be parameterized in CRMs. Most CRMs rely on bulk microphysics schemes to represent the complicated interactions between atmospheric thermodynamic states and hydrometeors and among various hydrometeor species. Bulk microphysics schemes typically divide the hydrometeor spectrum into cloud water, cloud ice, rain, and one or more ice-phase precipitation species (e.g. snow, graupel, and hail). Each hydrometeor class is represented by a specified size distribution function (e.g. gamma, exponential, and lognormal). The microphysics schemes that predict only hydrometeor mixing ratios are called the one-moment approach (e.g. Lin et al. 1983).

An improvement to the one-moment approach is to predict the rates of change for both mixing ratios and number concentrations of hydrometeors, i.e. the two-moment approach (e.g. Ferrier 1994; Meyers et al. 1997; Morrison et al. 2005, hereafter M05; Vaughan et al. 2007). An advantage of this approach is that the effective sizes of cloud particles, one of the most important parameters determining cloud radiative impacts, can be predicted, in contrast to the one-moment approach. Another advantage is that two-moment schemes potentially can represent the size distributions of hydrometeors more realistically and thus represent microphysical processes more accurately than one-moment schemes (e.g., Meyers et al. 1997; Morrison and Pinto 2006).

Arctic clouds have been identified as playing a central role in the Arctic climate system. However, the role of clouds is even less well understood in the Arctic than in other geographic regions, due to sparse observations. The Arctic field programs such as the Surface Heat Budget of the Arctic (SHEBA; Uttal et al. 2002) and the First ISCCP Regional Experiment (FIRE; where ISCCP is the International Satellite Cloud Climatology Program) Arctic Cloud Experiment (ACE; Curry et al. 2000) revealed that mixed-phase stratiform (MPS) clouds appear to dominate the low-cloud population within the Arctic (Intrieri et al. 2002). Moreover, it is found that the Arctic mixed-phase clouds are distinct from their lower latitude cousins (e.g. Curry et al. 1996, 2000). A unique feature of these clouds is that they are persistent, liquid-topped clouds that precipitate ice (Hobbs and Rangno 1998; Intrieri et al. 2002). Another unique feature of these clouds is that the liquid component of the mixed-phase cloud dominates the radiative properties (McFarquhar and Cober 2004; Zuidema et al. 2005)

Adequate simulation of Arctic clouds is needed to address Arctic cloud-radiative-surface interactions that may impact global climate (e.g. Curry et al. 1996) and to predict weather, due to the persistence and large horizontal extent of these cloud systems. However, there have been few simulations of Arctic MPS clouds with CRMs, primarily because the observations of cloud physical properties needed to evaluate model performance are sparse and there is a lack of large-scale forcing data available to drive CRMs. The Department of Energy - Atmospheric Radiation Measurement (DOE-ARM) Program (Stokes and Schwartz 1994; Ackerman and Stokes 2003)

recently launched its Mixed-Phase Arctic Cloud Experiment (M-PACE; September 27 - October 22, 2004) at the North Slope of Alaska (NSA) sites (Harrington and Verlinde 2004; Verlinde et al. 2007). During the field campaign, detailed information about Arctic clouds were measured using the ARM millimeter wave cloud radar, micropulse lidar, laser ceilometers, microwave radiometer (MWR), and three instrumented aircraft. Furthermore, the large-scale forcing data were derived for a seventeen and a half day Intensive Observation Period in October 2004 (Xie et al. 2006) by applying the method of Zhang and Lin (1997) and Zhang et al. (2001) to the available data. These forcing data can be used to drive models [CRMs, single-columns models (SCM; Randall et al. 1996), and large-eddy simulation (LES) models].

The objectives of this study are two-fold. One is to evaluate CRM simulations of Arctic MPS clouds with a state-of-the-art dataset. The available M-PACE data offer a promising opportunity for improving cloud microphysical parameterizations in CRMs. Here, single-layer MPS clouds observed during a sub-period of M-PACE are simulated using a CRM, driven by the ARM-derived large-scale forcing. The CRM includes a state-of-the-art radiative transfer scheme and either a one- or a two-moment microphysics scheme. The performance of the CRM is evaluated through comparing simulated cloud properties, such as the vertical profiles of cloud liquid water content (LWC), ice water content (IWC), droplet number concentration, ice number concentration, effective sizes of droplets and ice crystals, with the M-PACE aircraft observations (McFarquhar et al. 2007), as well as the retrievals of liquid water path (LWP; Turner et al. 2007) and observations of precipitation from ground-based instruments deployed at the NSA sites.

The second objective of this study is to explore the sensitivities of the simulated clouds to representation of various microphysical processes and parameters. To achieve this objective, a range of sensitivity tests are conducted. In particular, we attempt to answer the following questions: what differences in the simulated cloud properties are produced by use of a one- or two-moment microphysics approach? What microphysical processes and parameters may significantly influence the simulated MPS clouds?

Section 2 describes the CRM used in this study, with a focus on the prediction of hydrometeor number concentrations. Section 3 gives a description of the case and cloud-property observations. Design of the numerical experiments is presented in Section 4. Results from the CRM simulations utilizing either the one- or two-moment approach are compared with the aircraft measurements in Section 5. Section 6 contains results from the sensitivity tests. Summary and conclusions are given in Section 7.

2. The numerical model

The dynamic framework of the CRM used in this study is based on the anelastic forms of hydrostatic, momentum and continuity equations in two dimensions (x and z) with a third-moment turbulence closure (Krueger 1988; Xu and Krueger 1991). The CRM includes the Fu-Liou (1993) radiative transfer parameterization and either a one-moment or a two-moment microphysics parameterization. The two-moment bulk microphysics scheme of M05 has been implemented, which predicts the mixing ratios and number concentrations of cloud water, cloud ice, rain, and snow. The equations used to predict the hydrometeor number concentrations are:

$$\frac{dn_x}{dt} = -\frac{1}{\rho_0} \frac{\partial}{\partial z} (\rho_0 \overline{n_x'' w''}) + A_x + S_x + M_x \quad (1)$$

where n_x is the number concentration with the subscript x being c, i, r, s for cloud water, cloud ice, rain, and snow, respectively. ρ_0 is the dry air density of the initial (reference) state. $\overline{n_x'' w''}$ is the ensemble mean of the turbulent flux of n_x in the vertical direction. A_x refers to activation (for cloud water) and nucleation (for cloud ice), S_x represents sedimentation, and M_x denotes all other microphysical processes. The effects of turbulent fluctuations on number concentrations of raindrops and snow are ignored in the current version of the CRM, and the effects of turbulence

on their mixing ratios are also ignored (Krueger 1988). For number concentrations of cloud water and ice, K-theory is applied to determine the turbulence terms; that is,

$$\rho_0 \overline{n_x'' w''} = -\rho_0 K \frac{\partial n_x}{\partial z} \quad (2)$$

The exchange coefficient K is calculated using $K = cl\sqrt{TKE}$, where c is a constant (0.24), l is the turbulence length scale and TKE is the turbulent kinetic energy. Both l and TKE are determined by the third-moment turbulence closure (Krueger 1988).

Droplet activation is treated by a physically-based scheme (Abdul-Razzak et al. 1998; Abdul-Razzak and Ghan 2000). This scheme not only relates droplet activation to aerosol characteristics but also couples it with local cooling rate that is determined by cloud-scale and sub-grid turbulent vertical velocity as well as radiative cooling. The error of the parameterization is less than 10% under a wide variety of conditions (Abdul-Razzak et al. 1998; Abdul-Razzak and Ghan 2000). The turbulent upward motion for the droplet activation calculation is approximated as the square root of the vertical component of TKE per unit mass. Sedimentation of cloud particles is calculated with terminal particle fall velocities related to particle sizes and air density (Ikawa and Saito 1991). Parameterizations of all other microphysical processes follow M05, including deposition, condensation-freezing of ice nuclei, contact- and immersion-freezing nucleation of cloud droplet and raindrops, autoconversion of cloud water to rain and of cloud ice to snow, self-collection of cloud droplets and of raindrops, snow aggregation, accretion of cloud droplets, rain and cloud ice by snow, rime-splintering from accreted droplets and raindrops by snow, accretion of cloud water by rain, deposition/sublimation of cloud ice and snow, melting of snow, evaporation of rain and melted snow, saturation adjustment of cloud water, as well as the decrease in number concentrations during evaporation/sublimation.

In the M05 scheme, the gamma size distribution is assumed for cloud droplets and cloud ice crystals while the Marshall-Palmer (exponential) size distribution is used for raindrops and snowflakes. A gamma size distribution can be expressed as

$$N(D) = N_0 D^\mu e^{-\lambda D} \quad (3)$$

where D is diameter, N_0 is the “intercept” parameter, μ is the spectral shape parameter, and λ is the slope parameter. The value μ is determined by the relative radius dispersion (η ; defined as the ratio between the standard deviation and the mean radius):

$$\mu = 1/\eta^2 - 1 \quad (4)$$

Practically, parameters N_0 and λ can be diagnosed from the specified μ and predicted mixing ratio (q) and number concentration (n) of the species. That is, only μ needs to be specified using the two-moment approach. For the one-moment approach, two of the three parameters (N_0 , μ , and λ) need to be specified.

For cloud droplets, η is related to the number concentration, n_c , in the M05 scheme. However, the exact η - n_c relationships for Arctic clouds are not yet developed. There are currently only a few formulations relating η to n_c and these are based on observations at lower latitudes. For example, Rotstayn and Liu (2003; RL03) fitted three curves to measurements in polluted and unpolluted warm stratiform and shallow cumulus clouds. These curves are designed to represent the average variation of η with n_c , as well as lower and upper bounds of this variation. These curves shown in Fig. 1a are defined by

$$\eta = 1 - 0.7e^{-\alpha n_c} \quad (5)$$

where α equals 0.001 for the lower curve, 0.003 for the middle curve, and 0.008 for the upper curve. The corresponding μ - n_c relationships are displayed in Fig. 1b. The relationship of Eq. (5) with α of 0.003 is used in this study.¹ Note that there was considerable scatter in the data used by Rotstajn and Liu (2003) to obtain the η - n_c relationship of Eq. (5). Miles et al. (2000) created a database of stratus cloud droplet size distribution parameters, derived from in-situ data reported in the existing literature. The datasets included several parameters for 42 marine stratocumulus clouds and 52 continental stratocumulus clouds. These observations, however, do not show a systematic increase or decrease in η with increasing n_c . For cloud ice, a constant μ of 5 is used in M05, corresponding to a η of ~ 0.408 . Note that the Marshall-Palmer distribution is a special case of Eq. (4) with μ equal to zero. For the radiation calculation, the effective sizes of cloud water, cloud ice and snow are determined by the predicted size distributions.

The CRM also includes the commonly used one-moment bulk microphysics scheme of Lin et al. (1983) (L83 hereafter) with modifications to its ice-phase microphysics parameterization by Krueger et al. (1995). This scheme represents the rates of change of mixing ratios for five hydrometeor species (cloud water, cloud ice, rain, snow, and graupel) and is combined with an ice-water saturation adjustment (Lord et al. 1984) to determine the condensation/evaporation of cloud water and deposition/sublimation of cloud ice. Cloud water and cloud ice are assumed to be monodisperse. Precipitating hydrometeor species are assumed to have exponential size spectra. Number concentrations of the precipitating hydrometeor species can be diagnosed from the predicted mixing ratios and specified microphysical parameters

¹We also tested formulations for the spectral shape parameter (μ) as a function of n_c that were used in Grabowski (1998) and Morrison and Grabowski (2007). Figure 1 indicates that these formulations produce substantially different η at most values of n_c . For values of n_c of $\sim 60 \text{ cm}^{-3}$ simulated for this case study, however, the results are not sensitive to the specific formulation of μ . Therefore, these results are not included in this paper.

describing the hydrometeor size spectra. However, aerosol characterization is not physically linked to the hydrometeor number concentrations. For the radiation calculation, the effective radius of cloud droplet is specified (10 μm) and the effective sizes of cloud ice and snow are either empirically determined from IWC or specified (120 μm for snow), as in our earlier studies (Xu 2005; Luo et al. 2007).

The water-ice saturation adjustment scheme of Lord et al. (1984) requires assumptions about both the coexistence of cloud water and cloud ice at temperatures less than 0°C and the partitioning between condensation and deposition. Specifically, the Lord et al. scheme assumes that the saturation vapor mixing ratio q^* is a mass-weighted average of the respective saturation values over liquid water and ice at $-40^\circ\text{C} \leq T \leq 0^\circ\text{C}$ when both cloud water and cloud ice are present. Under subsaturated conditions, cloud water is evaporated first so that water vapor mixing ratio (q_v) would be equal to q^* . If subsaturated conditions are still present after all cloud water evaporates, enough cloud ice is sublimated such that $q_v \leq q^*$. On the other hand, production of either cloud water (Δq_c) or cloud ice (Δq_i) depends linearly on temperature under supersaturated conditions so that $\Delta q_c = q_v - q^*$ at $T = 0^\circ\text{C}$ and $\Delta q_i = q_v - q^*$ at $T = -40^\circ\text{C}$. A similar formulation was also developed by Tao et al. (1989) except for removing the iterative adjustment procedure used in Lord et al. (1984).

3. Description of the case study

The east-northeast flow brought cold near-surface air from the sea-ice located about 500 km north over the warm open ocean that was adjacent to the northern coast of Alaska (Fig. 2). The contrast between the cold-air and warm open ocean resulted in large ocean sensible and latent heat fluxes which, combined with the conditions of large-scale subsidence, promoted a well-mixed cloudy boundary layer. Single layer mixed-phase clouds were formed under these conditions (Verlinde et al. 2007). These clouds were then advected to the Alaskan coast where

they were observed at the ARM NSA sites -- Barrow and Oliktok Point (Fig. 2). The ARSCL (Active Remote Sensing of Clouds) algorithm (Clothiaux et al. 2000) derived cloud distribution exhibits the presence of single layer stratocumulus in the period 9-14 October, 2004 (not shown). The time-height distributions of radar reflectivity, lidar backscatter and lidar depolarization (e.g. Figure 6 of Verlinde et al. 2007) reveal the locations of cloud top and cloud liquid base, and the presence of shafts of ice precipitation and/or drizzle throughout the cloud layer and below cloud.

The bulk microphysical properties of the MPS clouds that occurred during M-PACE, i.e. total condensed water content, LWC, IWC, effective radius of supercooled water droplets, effective radius of ice crystals [defined following Fu (1996)], total water droplet number concentration and total ice crystal number concentration, were derived by McFarquhar et al. (2007) from measurements obtained by instruments on the University of North Dakota Citation aircraft. The Citation was equipped with a range of probes for measuring the size, shapes, and phases of the complete range of hydrometeors that can be sampled within a cloud. There were one Citation flights on October 9 and 12, respectively, and two on October 10, which occurred in single layer MPS clouds that were similar in structure. The four flights covered a period of ~ 6.5 h with about half of the period for in-cloud observation. Here the cloud base is defined as the lidar-derived liquid cloud bottom. The cloud top is defined as the cloud radar-derived cloud top or, when cloud radar data was not available, as the location where the total condensed water content became greater than 0.001 g m^{-3} (McFarquhar et al. 2007). The bulk properties are available at 10 s resolution, but represent a 30 s running average of the measured ice properties. There are 1131 in-cloud samples obtained from the four flights. The bulk cloud properties sampled by the four flights are used to validate model simulations in this study.

Other evaluation data include measurements of LWP provided by the microwave radiometer (MWR) (Turner et al. 2007) and those of surface precipitation provided at Barrow site. Large uncertainties, however, existed in the ARM surface precipitation measurements during M-

PACE because of both the blowing snow conditions and the lack of a dense observational network (Xie et al. 2006).

4. Design of CRM simulations

We conduct a set of simulations using the CRM described in Section 2 to explore the model ability to simulate the MPS clouds and its sensitivity to microphysics scheme and parameter. All these simulations start with the same initial profiles of the atmospheric state. They are prescribed with the same surface latent and sensible fluxes, large-scale subsidence, and horizontal advection of temperature and moisture. Details of forcing data are described in Section 4a. For the sensitivity simulations, different treatments of some microphysical processes and parameters, described in Section 4b, are used. The horizontal grid spacing is 2 km. The vertical grid spacing varies with height from 30 m to 102 m at heights below 1.9 km and is constant (500 m) above 1.9 km. The domain width is 256 km in the horizontal and 20 km in the vertical. A time step of 5 seconds is used for all simulations.

4.1 Initial conditions, large-scale forcing, and aerosol specification

The initial and lower boundary conditions, large-scale forcing data, and aerosol properties provided by Klein et al. (2006) are used in all simulations. The period of our simulation is from 17Z October 9 to 5Z October 10. The initial profiles of temperature and water vapor are based on the 17Z October 9 sounding at Barrow (Figs. 3a, b) with the inversion height at ~ 1.4 km. The CRM is initialized with an adiabatic profile of liquid water (Fig. 3b). No ice is present at the initial time. The total water mixing ratio below inversion is 1.95 g kg^{-1} . The CRM starts from horizontally homogeneous fields except for the added random perturbations with a maximum of 0.1 K to the potential temperature field at the lowest several levels.

The forcing data were based on an analysis of the ECMWF model data for the oceanic region adjacent to the NSA sites (Xie et al. 2006). The magnitude of the large-scale subsidence (ω) linearly increases with decreasing pressure from a zero value at the surface to a value of about

3.3 hPa h⁻¹ at and above the inversion (Fig. 3c). This is used to vertically advect all thermodynamic and microphysical variables in the model. The large-scale horizontal advective tendencies of temperature and moisture are also prescribed (Klein et al. 2006; also shown in Figs. 3d, e). Due to the lack of observations, the large-scale horizontal advective tendency of the cloud variables are set to zero. The CRM's horizontally-averaged winds (u and v) are also nudged toward the initial values (-13 m s⁻¹ for u and -3 m s⁻¹ for v , respectively) with a time scale of 1 h (Xu and Randall 1996). Surface sensible and latent heat fluxes are specified as 136.5 W m⁻² and 107.7 W m⁻², respectively. For radiation purposes, the lower boundary is an open-ocean surface. An SST of 274.01 K is used in the upward longwave radiation calculation. The spectral surface albedos for the six bands of Fu and Liou (1993) radiation code are calculated using the parameterization of Jin et al. (2004).

The CRM's droplet activation parameterization is physically linked to the characterization of aerosols. We use a bimodal lognormal size distribution of dry aerosol, obtained from a Met One Hand-Held Particle Counter (HHPC-6) on board the ARM unmanned aerial vehicle (UAV) and a condensation nuclei counter from the NOAA Earth System Research Laboratory located near Barrow, AK. The size distribution for each mode of the lognormal distribution is represented by

$$\frac{dN}{d\ln r} = \frac{N_t}{\sqrt{2\pi} \ln \sigma} \exp\left(-\frac{\ln^2(r/r_m)}{2 \ln^2 \sigma}\right) \quad (6)$$

where the parameters N_t , σ , and r_m are the total number concentration, standard deviation, and geometric mean radius of each mode, respectively. For the smaller mode, the values of these variables are 72.2 cm⁻³, 2.04, and 0.052 μ m, respectively. The corresponding values for the larger mode are 1.8 cm⁻³, 2.5, and 1.3 μ m. The aerosol composition is assumed to be ammonium bisulfate with an insoluble fraction of 30%, as recommended by Klein et al. (2006) based on observations (Bigg and Leck 2001; Zhou et al. 2001).

In-situ out-of-cloud observations for number concentration of active ice forming nuclei (IFN) were obtained on October 9 and 10 from the Continuous Flow Diffusion Chamber (Rogers et al. 2001) aboard the Citation aircraft. These measurements represent the total number concentration of active IFN that have diameters less than $2\text{ }\mu\text{m}$ acting in deposition, condensation-freezing, and immersion-freezing modes. The measured mean concentration of these IFN is about 0.16 L^{-1} , which is used to represent the aforementioned nucleation modes in the CRM simulations.

4.2 Sensitivity tests

In order to explore the possible impacts of microphysical processes and parameters on CRM-simulated MPS clouds, a range of sensitivity tests are performed (Table 1). The baseline simulation (hereafter referred to as CONTROL) is performed with a two-moment approach for both cloud particles and precipitating hydrometeor species using the M05 scheme. A sensitivity experiment, OneM, is performed with a one-moment approach for all hydrometeor species as described in Section 2 to quantify the benefits of the two-moment approach. Note that graupel is allowed to occur in the OneM simulation but it never does.

A sensitivity test (SAT), which is the same as the CONTROL except for using the water-ice saturation adjustment scheme of Lord et al. (1984), is designed to examine the role of the water-ice saturation adjustment used in the one-moment microphysics parameterization (Lord et al. 1984; Tao et al. 1989). The Lord adjustment scheme, described in Section 2, is different than the M05 scheme used in the CONTROL, which determines deposition/sublimation of cloud ice (as well as snow and rain) using a non-steady, vapor diffusion approach and applies a saturation adjustment approach only to cloud liquid water, which is reasonable because of short droplet phase relaxation time.

The rest of microphysics experiments test several microphysical parameters used in the M05 scheme. Experiment IN20 is performed by increasing the IFN number concentration by a factor of 20 from the measured value, i.e. from 0.16 L^{-1} to 3.2 L^{-1} . This experiment is motivated

by previous numerical modeling studies of Arctic MPS clouds which showed large sensitivity of simulated MPS clouds to the availability of IFN (Harrington et al. 1999; Jiang et al. 2000; Morrison and Pinto 2006). Morrison and Pinto (2006) found that the prediction of n_s could critically affect an MPS cloud simulated by a mesoscale numerical model. To examine this issue, experiment N0S is performed by setting the intercept parameter N_{0s} equal to a constant value of $3.0E6 \text{ m}^{-4}$ (Gunn and Marshall 1958; Lin et al. 1983) so that the number concentration of snow particles, n_s , is diagnosed rather than predicted. The last sensitivity test, $\mu i0$, examines the spectral shape parameter (μ) in the gamma size distribution (Eq. 4) of cloud ice in the two-moment approach. Experiment $\mu i0$ is performed with μ_i of zero, instead of 5 in the CONTROL. That is, cloud ice is represented by an exponential (rather than a gamma) size distribution in the $\mu i0$ experiment.

Another set of sensitivity tests (Table 1) aim at examining the impacts of estimated uncertainties in the surface fluxes, which are compared to the differences between the one-moment and two-moment schemes. These tests are the same as either the CONTROL or the OneM simulations, except for increasing or decreasing the surface sensible and latent heat fluxes, respectively, by 10%. One reason for performing these tests is that the magnitudes of these fluxes were based on the ECMWF model data for the oceanic region adjacent to the NSA sites and, therefore, may contain model uncertainties. Another reason is that previous modeling studies indicate that surface turbulent flux could influence properties of simulated mixed-phase Arctic clouds (e.g., Harrington and Olsson 2001).

5. Comparison between CRM simulations and aircraft observations

We first examine the CONTROL and OneM simulations since they represent results using the two distinct (two-moment vs. one-moment) microphysics schemes.

5.1 Vertical profiles of hydrometeor mass

The vertical profiles of LWC and IWC plus snow water content (hereafter, ISWC) from the CONTROL and OneM simulations and observations (means plus/minus standard deviations computed from the four flights) are compared to examine the vertical variations of cloud distributions. The simulated LWC and ISWC are horizontally averaged and time averaged at 30 min blocks during the 12 h simulation period. Only those centered at 3.25 h, 10.25 h, and 11.75 h are shown in Fig. 4. The observations represent both spatial and temporal variability since many of the observations were obtained in different locations (Barrow, Oliktok Point and in between). Following McFarquhar et al. (2007), the vertical axis of Fig. 4 is a normalized height (H_n) defined as $(H - H_b) / (H_t - H_b)$, where H is the height, H_b cloud base height and H_t cloud top height. The cloud top and cloud base are located at $H_n = 1$ and $H_n = 0$, respectively. A negative H_n represents a height below the liquid cloud base. Observations below liquid cloud base typically refer to the presence of precipitating ice, and on occasion refer to an erroneously identified cloud base. The observations are categorized into 20 bins of H_n within the cloud layer. There are about 50 samples for each of the observed cloud properties within each H_n bin.

McFarquhar et al. (2007) analyzed the variation of the observed microphysical variables with height. In order to compare against the model simulations, the most notable features are summarized here. The observed, averaged LWCs increase with height within the cloud layer with a peak of $\sim 0.32 \text{ g m}^{-3}$ located near the cloud top. The standard deviations of the observed LWC range from 0.05 g m^{-3} to 0.08 g m^{-3} below cloud top ($H_n < 0.8$) and increase to $\sim 0.14 \text{ g m}^{-3}$ at the cloud top. The larger variation of the observed LWC near cloud top may be related to entrainment. The observations also indicate that there is a small amount of ISWC (0.01 g m^{-3}) with a relatively constant vertical distribution within the cloud layer, but with large variations (up to 0.04 g m^{-3}) in the lower part of the cloud layer ($H_n < 0.25$). The large variations suggest that large ISWCs were only occasionally observed near cloud base. The observed fraction of ice to the total condensed water, however, increases towards the base of the cloud (McFarquhar et al. 2007).

The liquid and ice coexist throughout the entire period of the two simulations (Figs. 4a, b), consistent with the observations which showed mixed-phase clouds occurred 71% of the time for the observations. The cloud top and cloud base in the model are located at 1.33 km and 0.65 km, respectively. In both simulations, ice crystals (including snow) occur throughout the cloud layer and fall below liquid cloud base to the surface, consistent with radar and lidar measurements shown in Verlinde et al (2007). However, there are some obvious differences between the two simulations. In the CONTROL, both the LWC and the ISWC reach a steady state after ~ 3 h. The LWCs increase with height and the ISWCs are constant with height within the cloud layer. Both the LWC and ISWC are located within the uncertainty range of the observations. In the OneM experiment, the liquid cloud layer decays with time and the ice mass increases with time. The amount of LWC is underestimated compared to the observations. The ISWCs from the OneM experiment exhibit larger variations with height as well as larger amounts at most heights within the cloud layer than those in the observations or in the CONTROL results.

To further explore the differences in ice crystal mass between the CONTROL and OneM simulations, separate vertical profiles of IWC and snow water content (SWC) from the two simulations are compared (Figs. 4c, d). The IWCs from the CONTROL are nearly constant with height within the cloud layer. The IWCs from the OneM run exhibit two peaks, one located near the cloud top and the other at the lower part of the cloud layer during the majority of the 12 h simulation period. The only exception occurs at the last hour when there is a single peak at H_n of ~ 0.8 . These differences are related to the cloud ice deposition process in the CONTROL and OneM simulations, as shown in the time-height distributions of cloud ice deposition rate in Figs. 5a and b. In the CONTROL, deposition (from water vapor to cloud ice) occurs smoothly in height and in time within the cloud layer at the instantaneous rates of less than $0.01 \text{ g kg}^{-1} \text{ h}^{-1}$. In the OneM experiment, deposition (positive values) or sublimation (negative values) rates exhibit significant variability within the cloud layer, and are one order of magnitude larger than those seen in the CONTROL. The OneM simulation also produces deposition rates (in the lower part of the cloud layer) that oscillate with a period of about 30 minutes during the first 8 h of the

simulation. After cloud water decreases significantly in the OneM simulation (i.e. after 10 h of the simulation), the cloud ice deposition process is enhanced significantly within the cloud layer because the saturation vapor mixing ratio depends on the relative amounts of liquid and ice.

To examine the effects of microphysics on dynamics, the domain-averaged sub-grid turbulent kinetic energy (TKE) is compared between the CONTROL and OneM simulations (Figs. 5c, d). While the TKE produced by the CONTROL is relatively constant below the cloud top except for near the surface and changes little with time, the TKE produced in the OneM simulation shows more significant variability with time and height. The OneM TKE in the interior of the cloud layer oscillates with the same period as its deposition process does. The OneM TKE near the cloud base has smaller values than those in the interior of the cloud layer and below the cloud base. These results suggest that different representations of microphysics processes have distinct impacts on simulated dynamics.

Snow exists from the cloud top to the surface in both simulations with maxima located near the cloud base (Fig. 4d). However, the OneM experiment produced SWCs that are several times as large as those from the CONTROL. The larger SWCs in the OneM experiment are partly attributed to the greater deposition of cloud ice (Fig. 5b) that is subsequently converted to snow through the autoconversion process. As will be shown in Section 6, this result can also be attributed to the intercept parameter of the snow size distribution (N_{0s}) specified in the one-moment scheme, which is larger than that predicted in the CONTROL.

5.2 Vertical profiles of hydrometeor number concentration and effective radius

Number concentrations and effective radii of cloud liquid droplets and ice crystals are important cloud properties that significantly influence cloud optical properties and various microphysical processes. These variables are not predicted in the OneM experiment. Therefore, we compare those from the CONTROL simulation to the observations (Fig. 6). Averages of the observed droplet number concentrations (n_c) are relatively constant with height in the cloud layer with values of about 50 cm^{-3} (Fig. 6a). The variation of the observed n_c at each height bin ranges

from 20 to 35 cm^{-3} . The simulated n_c is constant with height and has a value of $\sim 60 \text{ cm}^{-3}$, generally consistent with and within the variability of the observations. The observations suggest that the effective radii of cloud droplets (r_e) generally increase with height within the cloud layer (Fig. 6b). The standard deviation of r_e ranges between 1 μm and 2 μm for most height bins except for near the cloud top where it increased to $\sim 3 \mu\text{m}$. The simulation reproduced the observed increase of r_e with height within the cloud layer. At most height bins, the simulated r_e is within the uncertainty range of the observations except for near the cloud base where the observations are greater than the simulated r_e . The underestimation of r_e near cloud base is probably related to the smaller simulated LWC at that height, compared to the observations (Fig. 4a). On the other hand, on some of the ramped ascents and descents there may have been some uncertainties in the identification of cloud base from the measurements.

The vertical profile of total ice crystal number concentration (n_i) from the observations (Fig. 6c) shows a relatively constant distribution with height with a mean of $1\text{-}3 \text{ L}^{-1}$, significantly greater than the observed IFN number concentration. The standard deviation of n_i is comparable to or greater than the mean value. The simulated n_i (including both cloud ice and snow) is less than 0.5 L^{-1} , smaller than the observed mean. Note that the observed n_i refers to concentration of ice particles with diameter greater than 50 μm . The discrepancy between the observed and simulated n_i would be even larger if ice particles with diameters smaller than 50 μm were excluded from the simulated results.

The observations show that the vertical profile of effective radius of ice crystals (r_{ei}), defined following Fu (1996), is constant with height and the mean values of r_{ei} are $\sim 25 \mu\text{m}$. In the CONTROL simulation, ice effective radius is calculated by mass-weighting of the inverse values for cloud ice and snow which also follow the definition of Fu (1996). The vertical profile of simulated r_{ei} is constant with height, consistent with the observations. However, the r_{ei} are greater

than the observed (60 μm versus 25 μm). This is due partly to simulated values of n_i that are smaller than the observed (Fig. 6c).

Underestimation of n_i was noticed in almost all models that participated in the ARM M-PACE model intercomparison (e.g. Fridlind et al. 2007). Reasons for this are not clear yet. The major ice forming mechanism in the CONTROL is contact-freezing of droplets. The 12 h averaged contact-freezing rate increases with height within the cloud layer from almost zero value to a value of $7 \times 10^{-6} \text{ g kg}^{-1} \text{ hr}^{-1}$ at the cloud top. The formation of ice by deposition, condensation-freezing and immersion freezing occurs near the cloud top with an averaged rate of $2 \times 10^{-6} \text{ g kg}^{-1} \text{ hr}^{-1}$. The best quantified mechanism for ice enhancement is probably the shedding of ice splinters during riming, i.e., the H-M mechanism (Hallett and Mossop 1974). However, ice splinter production through the H-M mechanism is not significant in the simulation because the cloud temperature ranges from -15 $^{\circ}\text{C}$ (cloud top) to -10 $^{\circ}\text{C}$ (cloud base), colder than the temperature necessary for the H-M mechanism to operate (-3 $^{\circ}\text{C}$ to -8 $^{\circ}\text{C}$). It is likely that other mechanisms for high ice particle concentration may be missing in the two-moment microphysics scheme. For example, Rangno and Hobbs (2001) argued that the fragmentation of delicate crystals (such as dendrites and aggregates) during crystal-crystal collisions and crystal-droplet collision and the shattering of some drops during freezing in free fall may play a role in the production of relatively high ice particle concentrations in Arctic clouds. Fridlind et al. (2007) claimed that two other mechanisms, formation of ice nuclei from drop evaporation residuals and drop freezing during evaporation, could be strong enough to account for the M-PACE observations.

6. Results from sensitivity experiments

We have shown that the CONTROL simulation reproduced most of the aircraft-observed cloud properties except for its underestimation of ice crystal number concentration and overestimation of ice crystal effective size. These two quantities have the largest uncertainties in

the observations (McFarquhar et al. 2007). The OneM experiment underestimated the observed LWC and produced a bimodal vertical structure of IWC that was not observed. Its simulated mixed-phase stratus glaciated earlier than in the CONTROL simulation. Four additional sensitivity experiments (Table 1), as described in Section 4b, are presented in this section to further explore the impact of microphysical processes and parameters on the simulated MPS clouds. Another set of sensitivity tests are used to explore the impacts of uncertainties in the surface fluxes, which are compared to the differences between the CONTROL and OneM simulations.

6.1 Vertically integrated hydrometeor amount

Figure 7 shows the time variability of the vertically integrated amount of each hydrometeor species, i.e. LWP, rain water path (RWP), ice water path (IWP), and snow water path (SWP) for the CONTROL, OneM, $\mu i0$, N0s, SAT and the IN20 simulation. The model results are averaged over the entire horizontal domain in space and 30 min in time. Time-averaged values and standard deviations of LWP, IWP, SWP and RWP between 4 h and 12 h from all simulations are given in Table 2.

A comparison among these simulations reveals the following major findings. First, a persistent MPS cloud layer is produced by the CONTROL, $\mu i0$, and N0S simulations, which reaches a steady state after 3 hr, although their steady state LWP values differ (176.5 ± 2.8 , 188.6 ± 4.4 , 142.6 ± 6.9 g m⁻², respectively). Second, both the OneM and SAT experiments produce smaller LWPs (54.2 ± 15.0 and 97.9 ± 12.1 g m⁻², respectively) than the other simulations shown in Fig. 7a. The temporal evolutions of IWP and SWP are similar between OneM and SAT, e.g. a large increase near the end of simulations (Figs. 7b and c). This behavior differs markedly from the other simulations. Third, the IN20 experiment produces smallest time-averaged LWP (8.0 ± 12.0 g m⁻²) but largest IWP (20.9 ± 13.2) and SWP (43.4 ± 5.6) among the simulations, with LWP decreasing monotonically with time until complete dissipation at 7 h. Detailed discussions of these findings are given below.

a. Effects of spectral shape parameter of cloud ice

The LWP derived from the MWR measurements averaged over the 12 h simulation period is 210 g m^{-2} at Barrow, which has an approximate $20\text{-}30 \text{ g m}^{-2}$ uncertainty (D. Turner 2007; personal communication). The steady-state LWP from the CONTROL, 176.5 g m^{-2} , is 84% of the retrievals. The $\mu\text{i}0$ experiment generated more LWP (188.6 vs. 176.5 g m^{-2}) and less IWP (1.5 vs. 4.4 g m^{-2}) and SWP (1.5 vs. 5.2 kg m^{-2}) compared to the CONTROL simulation. Decreasing the spectral shape parameter (μ_i) from 5 in the CONTROL simulation to zero in the $\mu\text{i}0$ experiment increases the phase relaxation time associated with cloud ice, i.e. making cloud ice deposition occur more slowly. The slower deposition to cloud ice at the expense of cloud water causes less IWP and SWP and more LWP in the $\mu\text{i}0$ experiment. Nevertheless, the difference in LWP between the two simulations is within the range of the uncertainties in the bulk observations that are presented.

b. Effects of predicting snow number concentration

Compared to the CONTROL, the N0S experiment produced less LWP (142.6 g m^{-2} vs. 176.5 g m^{-2}) and IWP (2.8 g m^{-2} vs. 4.4 g m^{-2}) but more SWP (25.8 g m^{-2} vs. 5.2 g m^{-2}). The joint PDF (%) of N_{0s} and height from the CONTROL (Fig. 8b) shows that the N_{0s} varies with height and is mostly one order of magnitude smaller than the specified constant value of $3 \times 10^6 \text{ m}^{-4}$ in the N0S experiment (Fig. 8a). Other simulations with predicted N_{0s} produced comparable values of N_{0s} to those produced by the CONTROL. The L83 value of N_{0s} used in the N0S experiment was obtained from mid-latitude frontal cloud system. Therefore, it is not surprising that this N_{0s} is different from that predicted in Arctic mixed-phase clouds. Snapshots of the predicted N_{0s} (not shown) exhibit horizontally inhomogeneous distributions that vary with time. The significantly larger N_{0s} used in the N0S experiment resulted in stronger depositional growth of snow (i.e. enhanced Bergeron-Findeisen mechanism) and more significant accretion of cloud droplets by

snow, both contributing to less LWP and more SWP. The smaller IWP with larger N_{0s} is due to more water vapor deposited to snow and therefore less to cloud ice.

Compared to the OneM experiment, the N0S experiment produced about the same SWP ($\sim 26 \text{ g m}^{-2}$) between 3 and 10 h, but less SWP after 10 h and higher LWP during most of the simulation period. The agreement in SWP between the OneM and N0S experiments for the 3-10 h period resulted from similar snow deposition rates and accretion rates of droplets by snow. The larger SWP in the OneM experiment after 10 h (up to 37 g m^{-2}) is related to its larger cloud ice deposition rates caused by the application of the water-ice saturation adjustment scheme of Lord et al. (1984) (Fig. 5b), and subsequently more cloud ice converted to snow. The smaller LWP of the OneM experiment versus the N0S experiment (54.2 vs. 142.6 g m^{-2}) is probably also a result from the water-ice saturation adjustment scheme utilized in the OneM experiment, as will be further explained below.

c. Effects of water-ice saturation adjustment

There are some similar results between the SAT and OneM simulations, i.e. an earlier decay of LWP and an increase of IWP and SWP after 9 h, compared to the other simulations shown in Figs. 7a-c. The relatively steady LWP between 3 h and 8 h has a magnitude of $\sim 100 \text{ g m}^{-2}$ in the SAT experiment compared to $\sim 177 \text{ g m}^{-2}$ for the CONTROL and $\sim 65 \text{ g m}^{-2}$ for the OneM simulation. Other aspects of hydrometeor paths simulated by SAT, such as the significant variabilities in LWP and SWP, are more similar to those from the OneM than the CONTROL (Table 2). These results suggest that the application of Lord et al. (1984) saturation adjustment in M05 to determine the condensation of cloud water and deposition of cloud ice could significantly change the simulated MPS clouds and could result in an underestimation of LWP. Why did the SAT experiment produce less LWP than the CONTROL? It is partly because condensation rates near the cloud top are smaller in the SAT simulation than in the CONTROL (Fig. 9). It is also due to more accretion by snow resulting from a greater amount of snow in the SAT experiment. Why did the SAT experiment produce less IWP and more SWP than the CONTROL? Deposition rates

in the SAT experiment (Fig. 9) are greater than those in the CONTROL, especially near the cloud base and cloud top, suggesting that more cloud ice is produced from deposition of water vapor and subsequently more efficient conversion from cloud ice to snow.

d. Effects of IFN number concentration

The IN20 experiment produces greater ice crystal number concentration ($\sim 3 L^{-1}$) than the CONTROL and much closer to the aircraft observations ($1-3 L^{-1}$; Fig. 6c). This is attained by increasing the IFN number concentration to 20 times of the measured value in the IN20 experiment. However, the increase in IFN number concentration (and hence increase in the ice crystal number concentration) transfers the solid, largely liquid stratus deck into a broken cloud system, consistent with previous modeling studies (Harrington et al. 1999; Jiang et al. 2000). As shown in Fig. 7e, the initially thick liquid cloud layer (LWP of $150 g m^{-2}$) decays monotonically with time in the IN20 experiment and is completely gone after 7 h. This is not realistic since a persistent cloud layer was observed. The decay of the simulated liquid cloud layer results from the significantly enhanced consumption of cloud water through the Bergeron processes when the ice crystal number concentration is increased in the simulation.

6.2 Precipitation and radiative flux at the surface

Arctic clouds are linked to the hydrological cycle and oceanic processes through precipitation that affects fresh water input into the Arctic ocean. Surface precipitation rate is therefore an important parameter to be reproduced by models. Frequent, light snow events were reported in the ARM ground measurements during the 9-14 October period. However, as mentioned in Section 3b, the ARM-observed surface precipitation rate could be overestimated because of blowing snow (Xie et al., 2006). The temporally averaged surface precipitation rate from the ARM observation at Barrow was $1.7 mm day^{-1}$ for the simulation period. Accumulated (horizontally-averaged) surface precipitation rates in the CRM simulations are shown in Table 3. The column denoted as “snow” represents the liquid water equivalent of the snow rate. The 12-h

averaged surface precipitation ranges from $\sim 0.3 \text{ mm day}^{-1}$ to 1.2 mm day^{-1} in the simulations, less than the ARM observations. The smallest 12-h averaged surface precipitation occurs in the $\mu i0$ and N0S experiments. However, the surface precipitation is mainly rain in the $\mu i0$ experiment and snow in the N0S experiment, respectively. The SAT and OneM experiments produce more surface precipitation in form of snow ($\sim 0.8 \text{ mm day}^{-1}$) than the other simulations ($< 0.3 \text{ mm day}^{-1}$) except for IN20 (1.1 mm day^{-1}), consistent with their more significant ice deposition rates. Note that rain does not occur in the OneM experiment because the threshold for activating the autoconversion parameterization from cloud water to rain is 0.5 g kg^{-1} , which is never reached. The IN20 experiment produces the largest surface precipitation among the simulations, due to the strong depositional growth of cloud ice and snow.

Differences in the representation of microphysical processes affect surface radiation budgets through their influences on the simulated cloud microphysical and optical properties. This is illustrated by the temporal variations of the half-hourly and horizontally averaged downwelling infrared (IR) and shortwave (SW) radiative fluxes (Fig. 10). A striking feature appearing in Fig. 10 is a dramatic reduction of the downwelling IR flux ($\sim 10 \text{ W m}^{-2} \text{ hr}^{-1}$) when the liquid water begins to decrease, i.e. after 6 h in the IN20 simulation, 10 h in the OneM simulation, and 11 h in the SAT experiment. The downwelling IR radiative fluxes in the CONTROL, $\mu i0$, and N0S simulations differ from one another by only $\sim 2 \text{ W m}^{-2}$ because these simulations all produced clouds that emitted as near blackbodies. The downward SW flux from the CONTROL has a maximal of $\sim 41 \text{ W m}^{-2}$ at 5-6 h, while those from the OneM and SAT simulations differ from the CONTROL by up to 25 W m^{-2} and 13 W m^{-2} , respectively.

6.3 Sensitivity to surface heat flux

Figure 11 shows the temporal variations of LWP, IWP, SWP, and RWP when surface heat fluxes are changed by $\pm 10\%$ with either the M05 or the L83 microphysics scheme. Comparisons are also made against those of the CONTROL and the OneM simulations. The 4 h to 12 h

averages and standard deviations of the vertically integrated water amounts are given in Table 2. With the M05 scheme, as expected, increasing the latent heat flux and decreasing sensible heat flux causes generally higher hydrometeor amounts, and *vice versa*. However, the effects of changing the surface fluxes are more complicated with the one-moment scheme with larger variabilities, which may be related to the oscillation in the OneM simulated TKE field (Fig. 5d). Most importantly, it is obvious that the differences caused by the two distinct microphysics schemes are more significant than those due to changes in the surface heat fluxes by 10%. For example, the time-averaged LWPs from the tests utilizing the M05 scheme range between 158.2 and 192.0 g m⁻² while those with the L83 scheme range between 51.2 and 58.5 g m⁻² (Table 2).

7. Summary and conclusions

There have been few CRM simulations of boundary layer MPS clouds even though these clouds occur frequently in the Arctic and may potentially impact global climate and regional weather. In this study, a CRM has been used to simulate single-layer MPS clouds observed at the NSA sites during the ARM M-PACE. This CRM was implemented with both a commonly used one-moment microphysics scheme (Lin et al. 1983) and an advanced two-moment microphysics scheme (Morrison et al. 2005) as well as a state-of-the-art radiative transfer scheme (Fu and Liou 1993). A set of simulations with different treatments of microphysical processes and different specifications of microphysical parameters were performed to examine the sensitivity of the CRM-simulated MPS clouds to cloud microphysics parameterizations. Modeled cloud fields have been compared to the vertical profiles of the bulk microphysical properties derived from aircraft measurements (McFarquhar et al. 2007), retrievals of LWP obtained from ground-based observations, as well as surface precipitation measurements.

The aircraft observations suggest that the LWCs and droplet effective radii increased with height in the cloud layer while the droplet number concentrations, and the masses, number concentrations and effective radii of ice crystals were relatively constant with height. Using the newly implemented two-moment scheme and the observed aerosol size distribution and IFN

number concentration, the CONTROL simulation was able to reproduce the magnitudes and vertical structures of cloud liquid water, cloud ice water, droplet number concentration, and droplet effective radius as revealed by the aircraft observations, although it underestimated the number concentration of the ice crystals by an order of magnitude and overestimated the effective radii of the ice crystals by a factor of 2-3. With the one-moment (OneM) microphysics scheme, the CRM produced values of LWP and ISWP that were about 30% and 4 times, respectively, of those produced by the CONTROL. In addition, the vertical profile of IWC exhibited a bimodal distribution in contrast to the constant distribution of IWC produced with the two-moment approach. The deficiencies in the OneM-simulated cloud fields are largely associated with the ice-water saturation adjustment of Lord et al. (1984), which overestimated ice deposition rate near the top and base of the MPS cloud layer. The deficiencies are also closely related to the constant large value of snow spectra intercept parameter (n_{0S}) used in Lin et al. (1983). Moreover, changing the surface latent and sensible heat fluxes, respectively, by 10%, which is an estimate of the possible uncertainties associated with these fluxes, caused smaller differences in the simulated cloud fields than those caused by application of the two- and one-moment microphysics schemes.

When the observed IFN number concentration was used, this CRM and many other models that participated in a model-intercomparison project (Klein et al. 2006, Fridlinde et al. 2007) could not reproduce the observed ice concentrations, which greatly exceeded those of ice nuclei (a few L^{-1} versus $0.16 L^{-1}$). On the other hand, the MPS clouds glaciated in the model when the ice concentration was initially close to the observed value, which was obtained by increasing the observed IFN number concentration by a factor of 20 ($0.16 L^{-1}$ to $3.2 L^{-1}$). The rapid glaciation of cloud liquid water through the enhanced Bergeron-Findeisen process at the higher ice number concentration in the CRM is consistent with previous modeling studies (Harrington et al. 1999; Jiang et al. 2000).

Results from a sensitivity test that used the Lord et al. (1984) water-ice saturation adjustment in the CONTROL simulation were more similar to those from the OneM simulation than the CONTROL. This indicates that the CRM-simulated MPS clouds are very sensitive to the

representations of cloud water condensation and cloud ice deposition. One of the major assumptions on which the saturation adjustment of Lord et al. (1984) is based, is that the saturation vapor mixing ratio (q^*) is a mass-weighted average of the respective saturation values over liquid and ice when both cloud water and cloud ice are present. Although this assumption was supported by the aircraft data collected during the SHEBA/FIRE-ACE campaign (Fu and Hollars 2004), its utilization in models is problematic since q^* depends on the model-simulated q_i and q_c and the accuracy of q_i and q_c prediction is influenced by other aspects of the model. Use of this assumption resulted in a significant underestimation of LWP during the fall season in an SCM simulation using SHEBA data (Yuan et al. 2006), qualitatively consistent with our findings.

It is found that the two-moment scheme predicted much smaller values of N_{0s} (mostly $< 0.5 \times 10^6 \text{ m}^{-4}$) than the constant value ($3 \times 10^6 \text{ m}^{-4}$) used in the one-moment scheme of Lin et al. (1983). The predicted N_{0s} from the two-moment approach varied with time and was both horizontally and vertically inhomogeneous. Using the constant larger N_{0s} resulted in 20% less LWP and 5 times more SWP. Furthermore, representing the cloud ice spectra with the exponential size distribution rather than the gamma distribution resulted in smaller IWP (1.5 vs. 4.4 g m^{-2}) and SWP (1.5 vs. 5.2 g m^{-2}) and larger LWP (188.6 vs. 176.5 g m^{-2}), due to a slower ice deposition process.

Note that the modeled results may be sensitive to some other parameters (such as the assumed bulk densities and fallspeeds of cloud ice and snow) involved in the two-moment microphysics scheme. The mechanisms for the formation of ice concentrations that greatly exceed those of ice nuclei in the MPS Arctic clouds and their representation in the models should be studied further. Additional observations and simulations are needed to further narrow down the uncertainties associated with these microphysical parameters because the conclusions drawn from this study have been based on only one case study.

Acknowledgments. Research of Y. Luo and K.-M. Xu was supported by the NASA CMAI as part of the Modeling, Analysis and Prediction Program (Dr. Donald Anderson, Program Manager) and partly supported by the Office of Biological and Environmental Research of the U.S. Department of Energy under interagency agreement DE-AI02-06ER64183, as part of the Atmospheric Radiation Measurement (ARM) Program. H. Morrison is grateful for support through the National Center for Atmospheric Research Advanced Study Program, sponsored by the National Science Foundation. Research of G. McFarquhar was supported by the Office of Biological and Environmental Research of the U.S. Department of Energy (DE-FG02-02ER63337) as part of the ARM Program. Data were obtained from the ARM program archive, sponsored by the Office of Biological and Environmental Research of the U.S. Department of Energy. The authors thank Drs. Anthony Prenni and Paul DeMott of Colorado State University for providing the IFN measurements. Drs. Takmeng Wong and Zachary A. Eitzen of NASA Langley Research Center are appreciated for reading the manuscript and making useful comments.

References

- Abdul-Razzak, H., and S. J. Ghan, 2000: A parameterization of aerosol activation. 2. Multiple aerosol types. *J. Geophys. Res.*, **105**, 6837-6844.
- Abdul-Razzak, H., S. J. Ghan, and C. Rivera-Carpio, 1998: A parameterization of aerosol activation. 1. Single aerosol types. *J. Geophys. Res.*, **103**, 6123-6131.
- Ackerman, T., and G. Stokes, 2003: The Atmospheric Radiation Measurement Program. *Phys. Today*, **56**, 38-45.
- Arakawa, A., 2004: The cumulus parameterization problem: Past, present, and future. *J. Climate*, **17**, 2493-2525.
- Bigg, E. K., and C. Leck, 2001: Cloud active particles over the central Arctic Ocean. *J. Geophys. Res.*, **106**, 32155-32166.
- Clothiaux, E. E., T. P. Ackerman, G. G. Mace, K. P. Moran, R. T. Marchand, M. Miller, and B. E. Martner, 2000: Objective determination of cloud heights and radar reflectivity using a combination of active remote sensors at the ARM CART Sites. *J. Appl. Meteor.*, **39**, 645-665.
- Curry, J. A., W. B. Rossow, and J. L. Schramm, 1996: Overview of Arctic cloud and radiation properties. *J. Climate*, **9**, 1731-1764.
- Curry, J. A., and Coauthors, 2000: FIRE Arctic Clouds Experiment. *Bull. Amer. Meteor. Soc.*, **81**, 5-29.

- Ferrier, B. S., 1994: A double-moment multiple-phase four-class bulk ice scheme. Part I: Description. *J. Atmos. Sci.*, **51**, 249-280.
- Fridlind, A. M., A. S. Ackerman, G. McFarquhar, G. Zhang, M. R. Poellot, P. J. DeMott, A. J. Prenni, and A. J. Heymsfield, 2007: Ice properties of single-layer stratocumulus during the Mixed-Phase Arctic Cloud Experiment (M-PACE): Part II, Model results. Submitted to *J. Geophys. Res.*
- Fu, Q., 1996: An accurate parameterization of the solar radiative properties of cirrus clouds for climate models. *J. Climate*, **9**, 2058-2082.
- Fu, Q., and S. Hollars, 2004: Testing mixed-phase cloud water vapor parameterizations with SHEBA/FIRE-ACE observations. *J. Atmos. Sci.*, **61**, 2083-2091.
- Fu, Q., and K. N. Liou, 1993: Parameterization of the radiative properties of clouds. *J. Atmos. Sci.*, **50**, 2008-2025.
- Grabowski, W. W., 1998: Toward cloud-resolving modeling of large-scale tropical circulations: A simple cloud microphysics parameterization. *J. Atmos. Sci.*, **55**, 3283-3298.
- Grabowski, W. W., 2003: MJO-like coherent structures: Sensitivity simulations using the cloud-resolving convection parameterization (CRCP). *J. Atmos. Sci.*, **58**, 978-997.
- Gunn, K. L. S., and J. S. Marshall, 1958: The distribution with size of aggregate snowflakes. *J. Meteor.*, **15**, 452-461.

- Hallett, J., and S. C. Mossop, 1974: Production of secondary particles during the riming process. *Nature*, **249**, 26-28.
- Harrington, J., and P. Q. Olsson, 2001: On the potential influence of ice nuclei on surface-forced marine stratocumulus cloud dynamics. *J. Geophys. Res.*, **106**(D21), 27473-27486, 10.1029/2000JD000236.
- Harrington, J., and J. Verlinde, 2004: Mixed-phase Arctic Clouds Experiment (M-PACE): The ARM scientific overview document, report, 20pp., U.S. Dep. of Energy, Washington, D. C.
- Harrington, J. Y., T. Reisin, W. R. Cotton, and S. M. Kreidenweis, 1999: Cloud resolving simulations of Arctic stratus. Part II: Transition-season clouds. *Atmos. Res.*, **55**, 45-75.
- Hobbs, P. V., and A. L. Rangno, 1998: Microstructure of low and middle-level clouds over the Beaufort Sea. *Q. J. R. Meteor. Soc.*, **124**, 2035-2071.
- Ikawa, M., and K. Saito, 1991: Description of a nonhydrostatic model developed at the Forecast Research Department of the MRI. Meteorological Institute Tech. Rep. 28, 238 pp.
- Intrieri, J. M., M. D. Shupe, T. Uttal, and B. J. McCarty, 2002: An annual cycle of Arctic cloud characteristics observed by radar and lidar at SHEBA. *J. Geophys. Res.*, **107**, 8029, doi:10.1029/2000JC000423.
- Jiang, H., W. R. Cotton, J. O. Pinto, J. A. Curry, and M. J. Weissbluth, 2000: Cloud resolving simulations of mixed-phase Arctic stratus observed during BASE: Sensitivity to

- concentration of ice crystals and large-scale heat and moisture advection. *J. Atmos. Sci.*, **57**, 2105-2117.
- Jin, Z., T. Charlock, W. Smith, Jr., and K. Rutledge, 2004: A parameterization of ocean surface albedo. *Geophys. Res. Lett.*, **31**, L22301, doi:10.1029/2004GL021180.
- Klein, S., A. Fridlind, R. McCoy, G. McFarquhar, S. Menon, H. Morrison, S. Xie, J. J. Yio, and M. Zhang, 2006: ARM Cloud Parameterization and Modeling Working Group - GCSS Polar Cloud Working Group model intercomparison. Procedures for ARM CPMWG Case 5/ GCSS Polar Cloud WG SCM/CRM/LES Intercomparison Case f2004: ARM Mixed-phase Arctic Cloud Experiment (M-PACE): October 5-22, 2004. Available at <http://science.arm.gov/workinggroup/cpm/scm/scmic5/index.html>.
- Krueger, S. K., 1988: Numerical simulation of tropical cumulus clouds and their interaction with the subcloud layer. *J. Atmos. Sci.*, **45**, 2221-2250.
- Krueger, S. K., Q. Fu, K. N. Liou, and H.-N. S. Chin, 1995: Improvements of an ice-phase microphysics parameterization for use in numerical simulations of tropical convection. *J. Appl. Meteor.*, **34**, 281-287.
- Lin, Y. L., R. D. Farley, and H. D. Orville, 1983: Bulk parameterization of the snow field in a cloud model. *J. Climate Appl. Meteor.*, **22**, 1065-1092.
- Lord, S. J., H. E. Willoughby, and J. M. Piotrowicz, 1984: Role of a parameterized ice-phase microphysics in an axisymmetric tropical cyclone model. *J. Atmos. Sci.*, **41**, 2836-2848.

- Luo, Y., K.-M. Xu, B. A. Wielicki, T. Wong, and Z. A. Eitzen, 2007: Statistical analyses of satellite cloud object data from CERES. Part III: Comparison with cloud-resolving model simulations of tropical convective clouds. *J. Atmos. Sci.*, **64**, 762-785.
- McFarquhar, G. M., and S. G. Cober, 2004: Single-scattering properties of mixed-phase Arctic clouds at solar wavelengths: impacts on radiative transfer. *J. Climate*, **17**, 3799-3813.
- McFarquhar, G. M., G. Zhang, M. Poellot, J. Verlinde, G. Kok, R. McCoy, T. Tooman, and A. J. Heymsfield, 2007: Ice properties of single-layer stratocumulus during the Mixed-Phase Arctic Cloud Experiment (M-PACE): Part I, Observations. Submitted to *J. Geophys. Res.*
- Meyers, M. P., R. L. Walko, J. Y. Harrington, and W. R. Cotton, 1997: New RAMS cloud microphysics parameterization. Part II: The two-moment scheme. *Atmos. Res.*, **45**, 3-39.
- Miles, N. L., J. Verlinde, and E. E. Clothiaux, 2000: Cloud droplet size distributions in low-level stratiform clouds. *J. Atmos. Sci.*, **57**, 295-311.
- Morrison, H., and W. W. Grabowski, 2007: Comparison of bulk and bin warm rain microphysics models using a kinematic framework. *J. Atmos. Sci.* (in press).
- Morrison, H., and J. O. Pinto, 2006: Intercomparison of bulk cloud microphysics schemes in mesoscale simulations of springtime Arctic mixed-phase stratiform clouds. *Mon. Wea. Rev.*, **134**, 1880-1900.

- Morrison, H., J. A. Curry, and V. I. Khvorostyanov, 2005: A new double-moment microphysics parameterization for application in cloud and climate models. Part I: Description. *J. Atmos. Sci.*, **62**, 1665-1677.
- Randall, D., K.-M. Xu, R. J. C. Somerville, and S. Iacobellis, 1996: Single-column models and cloud ensemble models as links between observations and climate models. *J. Climate*, **9**, 1683-1697.
- Randall, D. A., and Coauthors, 2003: Confronting models with data. The GEWEX Cloud System Study. *Bull. Amer. Meteor. Soc.*, **84**, 455-469.
- Rangno, A. L., and P. V. Hobbs, 2001: Ice particles in stratiform clouds in the Arctic and possible mechanisms for the production of high ice concentrations. *J. Geophys. Res.*, **106**, 15,065-15,075.
- Rogers, D. C., P. J. DeMott, S. M. Kreidenweis, and Y. Chen, 2001: A continuous-flow diffusion chamber for airborne measurements of ice nuclei. *J. Atmos. Ocean. Technol.*, **18**, 725-741.
- Rotstayn, L. D., and Y. Liu, 2003: Sensitivity of the first indirect aerosol effect to an increase of cloud droplet spectral dispersion with droplet number concentration. *J. Climate*, **16**, 3476-3481.
- Skamarock, W. C., J. B. Klemp, J. Dudhia, D. O. Gill, D. M. Marker, W. Wang, and J. G. Powers, 2005: A description of the advanced research WRF version 2. [Available at <http://www.wrf-model.org/wrfadmin/publications.php>]

- Stokes, G. M., and S. E. Schwartz, 1994: The Atmospheric Radiation Measurement (ARM) Program: Programmatic background and design of the Cloud and Radiation Test Bed. *Bull. Amer. Meteor. Soc.*, **75**, 1201-1221.
- Tao, W.-K., J. Simpson, and M. McCumber, 1989: An ice-water saturation adjustment. *Mon. Wea. Rev.*, **117**, 231-235.
- Tomita, H., H. Miura, S. Iga, T. Nasuno, and M. Satoh, 2005: A global cloud-resolving simulation: Preliminary results from an aqua planet experiment. *Geophys. Res. Lett.*, **32**, L08805, doi:10.1029/2005GL022459.
- Turner, D. D., S. A. Clough, J. C. Liljegren, E. E. Clothiaux, K. Cady-Pereira, and K. L. Gaustad, 2007: Retrieving liquid water path and precipitable water vapor from Atmospheric Radiation Measurement (ARM) microwave radiometers. *IEEE Trans. Geosci. Remote Sens.*, submitted.
- Uttal, T., and Coauthors, 2002: The surface heat budget of the Arctic Ocean. *Bull. Amer. Meteor. Soc.*, **83**, 255-275.
- Vaughan, P. L., J. Donner, and S. Garner, 2007: Nucleation processes in deep convection simulated by a cloud-system resolving model with double-moment bulk microphysics. *J. Atmos. Sci.* (in press)
- Verlinde, J., and coauthors, 2007: The Mixed-Phase Arctic Cloud Experiment (M-PACE). *Bull. Amer. Met. Soc.*, **88**, 205-221.

- Xie S., S. A. Klein, M. Zhang, J. J. Yio, R. T. Cederwall, and R. McCoy, 2006: Developing large-scale forcing data for single-column and cloud-resolving models from the Mixed-Phase Arctic Cloud Experiment. *J. Geophys. Res.*, **111**, D19104, doi:10.1029/2005JD006950.
- Xu, K.-M., 2005: The sensitivity of diagnostic radiative properties to cloud microphysics among cloud-resolving model simulations. *J. Atmos. Sci.*, **62**, 1241-1254.
- Xu, K.-M., and S. K. Krueger, 1991: Evaluation of cloudiness parameterizations using a cumulus ensemble model. *Mon. Wea. Rev.*, **119**, 342-367.
- Xu, K.-M., and D. A. Randall, 1996: Explicit simulation of cumulus ensembles with the GATE phase III data: Comparison with observations. *J. Atmos. Sci.*, **53**, 3710-3736.
- Yuan, J., Q. Fu, and N. McFarlane, 2006: Test and improvements of GCM cloud parameterizations using the CCCMA SCM with the SHEBA data set. *Atmos. Res.*, **82**, 222-238.
- Zhang, M. H., and J. L. Lin, 1997: Constrained variational analysis of sounding data based on column-integrated budgets of mass, heat, moisture, and momentum: Approach and application to ARM measurements. *J. Atmos. Sci.*, **54**, 1503-1524.
- Zhang, M. H., J. L. Lin, R. T. Cederwall, J. J. Yio, and S. C. Xie, 2001: Objective analysis of ARM IOP data: Method and sensitivity. *Mon. Wea. Rev.*, **129**, 295-311.

Zhou, J., E. Swietlicki, O. H. Berg, P. P. Aalto, K. Hameri, E. D. Nilsson, and C. Leck, 2001:

Hygroscopic properties of aerosol particles over the central Arctic Ocean during summer.

J. Geophys. Res., **106**, 32111-32124.

Zuidema, P., B. Baker, Y. Han, J. Intrieri, J. Key, P. Lawson, S. Matrosov, M. Shupe, R. Stone, and

T. Uttal, 2005: An Arctic springtime mixed-phase cloudy boundary layer observed

during SHEBA. *J. Atmos. Sci.*, **62**, 160-176.

Table 1: Description of the CRM simulations.

	Microphysics
CONTROL	M05
OneM	Lin83 combined with Lord et al. (1984) and Krueger et al. (1995)
SAT	M05 combined with Lord et al. (1984)
IN20	same as CONTROL except IFN number concentration increased to 3.2 L^{-1}
μ_{i0}	same as CONTROL except an exponential distribution is assumed for cloud ice
N0s	same as CONTROL except for n_s is diagnosed
CTR.LH+	same as CONTROL except for increasing surface latent heat flux by 10%
CTR.LH-	same as CONTROL except for decreasing surface latent heat flux by 10%
CTR.SH+	same as CONTROL except for increasing surface sensible heat flux by 10%
CTR.SH-	same as CONTROL except for decreasing surface sensible heat flux by 10%
1M.LH+	same as OneM except for increasing surface latent heat flux by 10%
1M.LH-	same as OneM except for decreasing surface latent heat flux by 10%
1M.SH+	same as OneM except for increasing surface sensible heat flux by 10%
1M.SH-	same as OneM except for decreasing surface sensible heat flux by 10%

Table 2. The simulated LWP, IWP, SWP, and RWP (g m^{-2}) averaged between 4 h and 12 h. The numbers before and after “ \pm ” are the means and standard deviations, respectively.

	LWP	IWP	SWP	RWP
CONTROL	176.5 \pm 2.8	4.4 \pm 0.1	5.2 \pm 0.9	8.5 \pm 0.5
OneM	54.2 \pm 15.0	4.7 \pm 1.6	28.7 \pm 4.6	0.0 \pm 0.0
SAT	97.9 \pm 12.1	4.6 \pm 0.2	16.0 \pm 5.6	0.3 \pm 0.0
IN20	8.0 \pm 12.0	20.9 \pm 13.2	43.4 \pm 5.6	0.0 \pm 0.0
$\mu\text{i}0$	188.6 \pm 4.4	1.5 \pm 0.4	1.5 \pm 0.3	11.0 \pm 0.8
N0s	142.6 \pm 6.9	2.8 \pm 0.1	25.8 \pm 0.7	1.2 \pm 0.2
CTR.LH+	192.0 \pm 4.1	4.5 \pm 0.2	6.2 \pm 1.2	11.9 \pm 0.8
CTR.LH-	158.2 \pm 4.1	4.4 \pm 0.2	4.3 \pm 0.7	5.4 \pm 0.7
CTR.SH+	163.4 \pm 2.5	4.0 \pm 0.1	6.3 \pm 0.9	6.3 \pm 0.5
CTR.SH-	184.9 \pm 3.6	4.8 \pm 0.2	5.5 \pm 0.7	9.9 \pm 0.5
1M.LH+	58.0 \pm 17.1	4.8 \pm 1.4	32.2 \pm 4.5	0.0 \pm 0.0
1M.LH-	51.2 \pm 14.3	3.7 \pm 1.3	24.6 \pm 2.4	0.0 \pm 0.0
1M.SH+	58.5 \pm 13.2	5.2 \pm 1.1	27.7 \pm 1.4	0.0 \pm 0.0
1M.SH-	55.2 \pm 10.3	4.3 \pm 1.2	27.9 \pm 3.9	0.0 \pm 0.0

Table 3. Surface precipitation rates averaged over the entire 12-h and 3-h to 12-h simulation periods, respectively.

(mm/day)	rain		snow		rain plus snow	
	0h-12 h	3h-12h	0h-12h	3h-12h	0h-12h	3h-12h
CONTROL	0.23	0.18	0.17	0.20	0.39	0.38
$\mu i0$	0.28	0.24	0.02	0.02	0.30	0.27
N0s	0.03	0.00	0.27	0.30	0.30	0.30
SAT	0.06	0.00	0.83	0.76	0.89	0.76
OneM	0.00	0.00	0.76	0.71	0.76	0.71
IN20	0.05	0.00	1.13	1.28	1.19	1.28

Figure Caption

Figure 1. (a) The η - n_c relationships represented by Eq. (5) in the text: short dashed line represents RL03 with α being 0.003; dot-dashed lines represent RL03 \pm with α being 0.001 and 0.008, respectively. Also shown are the formulations from Morrison and Grabowski (2007) (solid line) and Grabowski (1998) (long dashed line). (b) The corresponding μ - n_c relationships. See text for further explanation.

Figure 2. Composite visible satellite image from the NASA Terra satellite for October 9, 2004. The dots indicate the locations of the ARM sites at the North Slope of Alaska: Barrow, Oliktok Point, and Atkasuk.

Figure 3. The upper panels show profiles of potential temperature (a), water vapor mixing ratio (q_v) and cloud water mixing ratio (q_c) (b) at the initial time of the simulations. The lower panels show profiles of the large-scale vertical velocity (c), and horizontal advective tendencies of temperature (d) and moisture (e), respectively.

Figure 4. Vertical profiles of liquid water content (a) and total ice water content (b) from the aircraft observations (black solid lines representing the means and shadows representing plus and minus one standard deviation), the CONTROL simulation (red lines) and the OneM simulation (blue lines). Vertical profiles of ice water content (c) and snow water content (d) from the CONTROL simulation (red lines) and the OneM simulation (blue lines). Three lines are shown for each of the simulation in each panel: long dashed line 3.25 hr, short dashed line 10.25 hr, and dot-dashed line 11.75 hr.

Figure 5. Time-height distribution of ice deposition rate ($\text{g kg}^{-1} \text{ hr}^{-1}$) sampled at 5-min interval from the CONTROL (a) and OneM (b) simulations, respectively. Panels (c) and (d) are the same as (a) and (b) except for turbulent kinetic energy ($\text{m}^2 \text{ s}^{-2}$)

Figure 6. Vertical profiles of droplet number concentration (a), droplet effective radius (b), ice crystal number concentration (c), and ice crystal effective radius (d) from the CONTROL

simulation (dashed lines) and the aircraft observations (solid lines representing the means and shadows representing plus and minus one standard deviation).

Figure 7. Time series of LWP (a), IWP (b), SWP (c), and RWP (d) produced by CRM simulations: CONTROL (solid), N0S (dots-dashed), $\mu i0$ (dotted), SAT (dot-dashed), and OneM (long-dashed with diamonds). Panel (e) represents time series of LWP (solid line), IWP (long dashed line), SWP (short dashed line), IWC plus SWP (dot-dashed line) and RWP (dots-dashed line) produce by the IN20 experiment.

Figure 8. (a) Frequency distribution of N_{0s} predicted by the CONTROL simulation. (b) Joint PDF (%) of N_{0s} and height predicted by the CONTROL simulation. The contours from light to dark represent 0.1%, 0.5%, 1.0%, and 2.0%.

Figure 9. Vertical profiles of cloud water condensation (solid lines) and cloud ice deposition (dashed lines) averaged over the 12-hr period of the CONTROL (left) and SAT (right) simulations, respectively. The dotted lines represent the cloud boundaries.

Figure 10. Time-series of the half-hourly and horizontally averaged downwelling infrared (a) and shortwave (b) radiative flux at the surface in the CRM simulations. Panels (c) and (d) represent the differences between the sensitivity simulations and the CONTROL.

Figure 11. Time-series of horizontally averaged LWP (a, e), IWP (b, f), SWP (c, d), and RWP (d, h) from the experiments with the surface latent heat flux increased (long dashed lines) or decreased (short dashed lines) by 10%, or with the surface sensible heat flux increased (dot-dashed lines) or decreased (dotted lines) by 10%, respectively. Left panels: with the M05 scheme. Right panels: with the L83 scheme. The solid lines represent results from the CONTROL (left panels) and OneM (right panels) simulations.

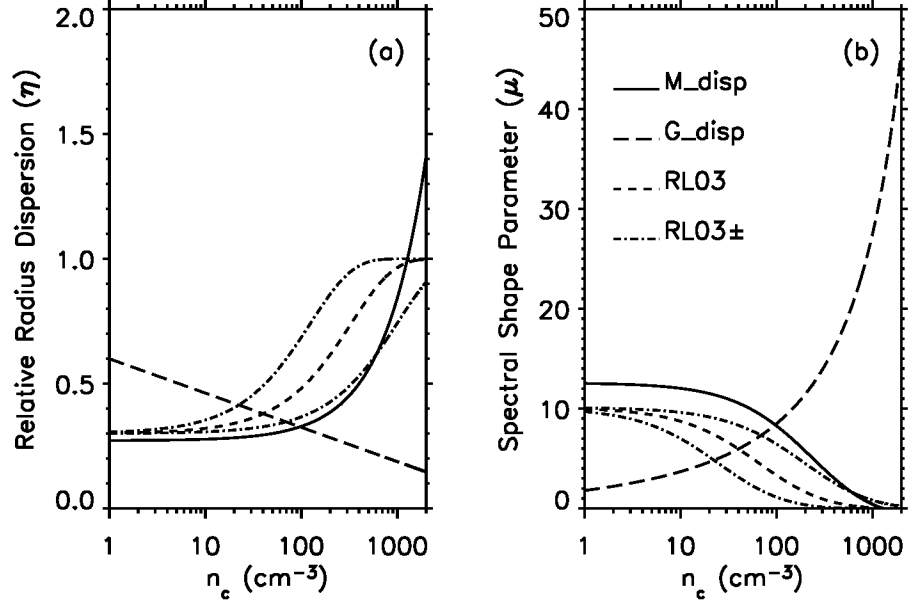


Figure 1. (a) The η - n_c relationships represented by Eq. (5) in the text: short dashed line represents RL03 with α being 0.003; dot-dashed lines represent RL03± with α being 0.001 and 0.008, respectively. Also shown are the formulations from Morrison and Grabowski (2007) (solid line) and Grabowski (1998) (long dashed line). (b) The corresponding μ - n_c relationships. See text for further explanation.

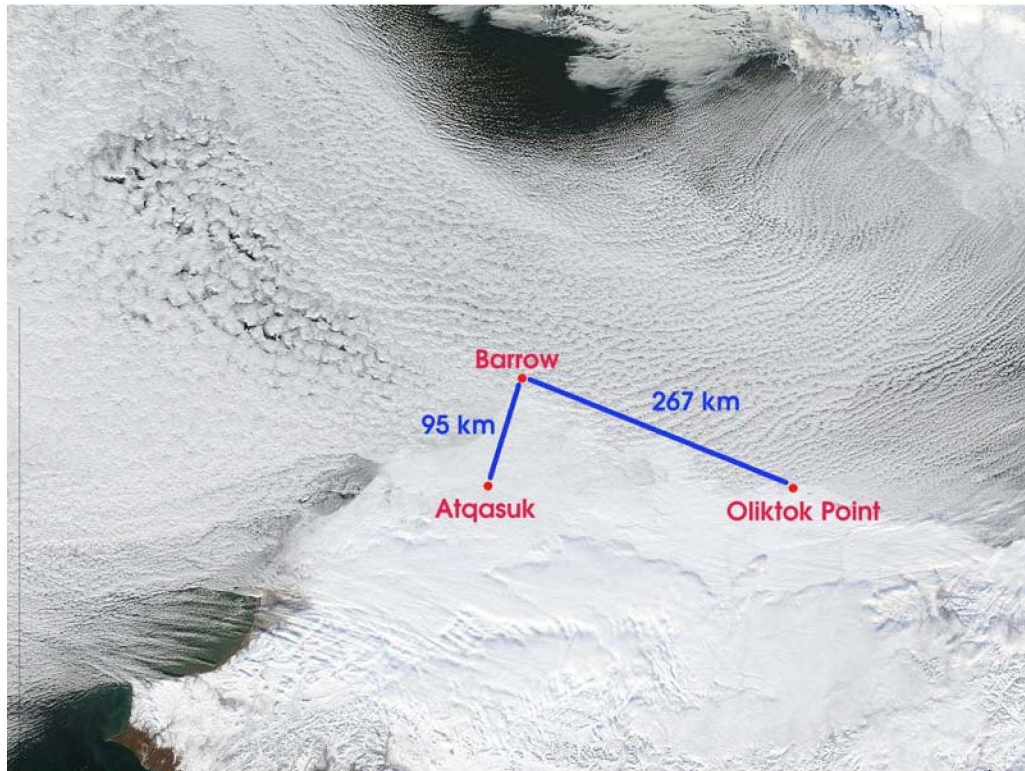


Figure 2. Composite visible satellite image from the NASA Terra satellite for October 9, 2004. The dots indicate the locations of the ARM sites at the North Slope of Alaska: Barrow, Oliktok Point, and Atqasuk.

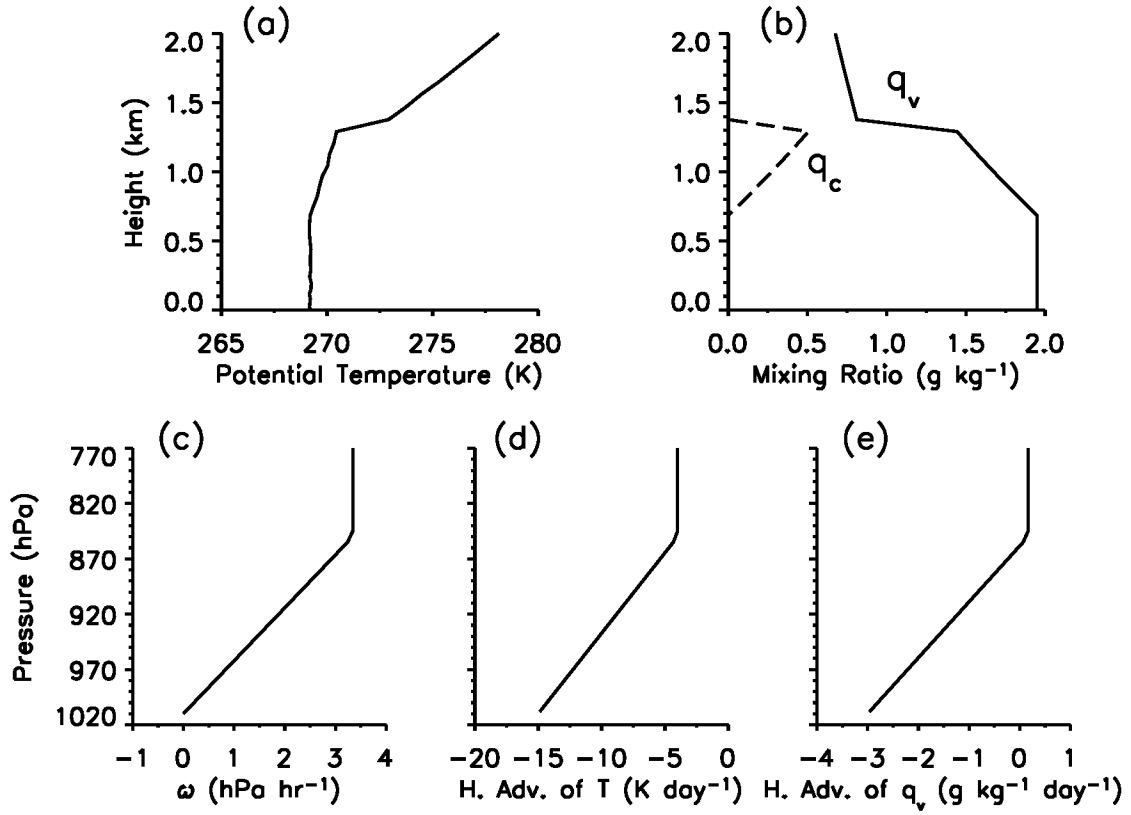


Figure 3. The upper panels show profiles of potential temperature (a), water vapor mixing ratio (q_v) and cloud water mixing ratio (q_c) (b) at the initial time of the simulations. The lower panels show profiles of the large-scale vertical velocity (c), and horizontal advective tendencies of temperature (d) and moisture (e), respectively.

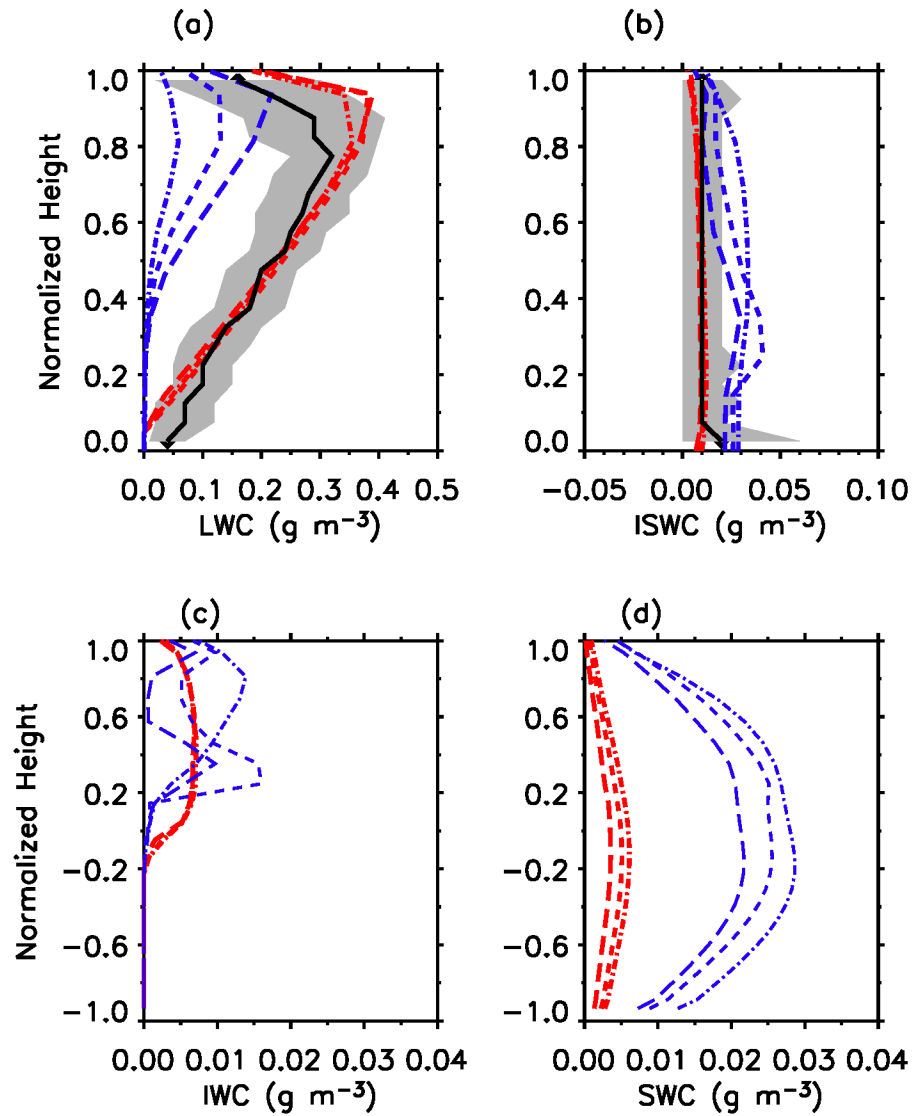


Figure 4. Vertical profiles of liquid water content (a) and total ice water content (b) from the aircraft observations (black solid lines representing the means and shadows representing plus and minus one standard deviation), the CONTROL simulation (red lines) and the OneM simulation (blue lines). Vertical profiles of ice water content (c) and snow water content (d) from the CONTROL simulation (red lines) and the OneM simulation (blue lines). Three lines are shown for each of the simulation in each panel: long dashed line 3.25 hr, short dashed line 10.25 hr, and dot-dashed line 11.75 hr.

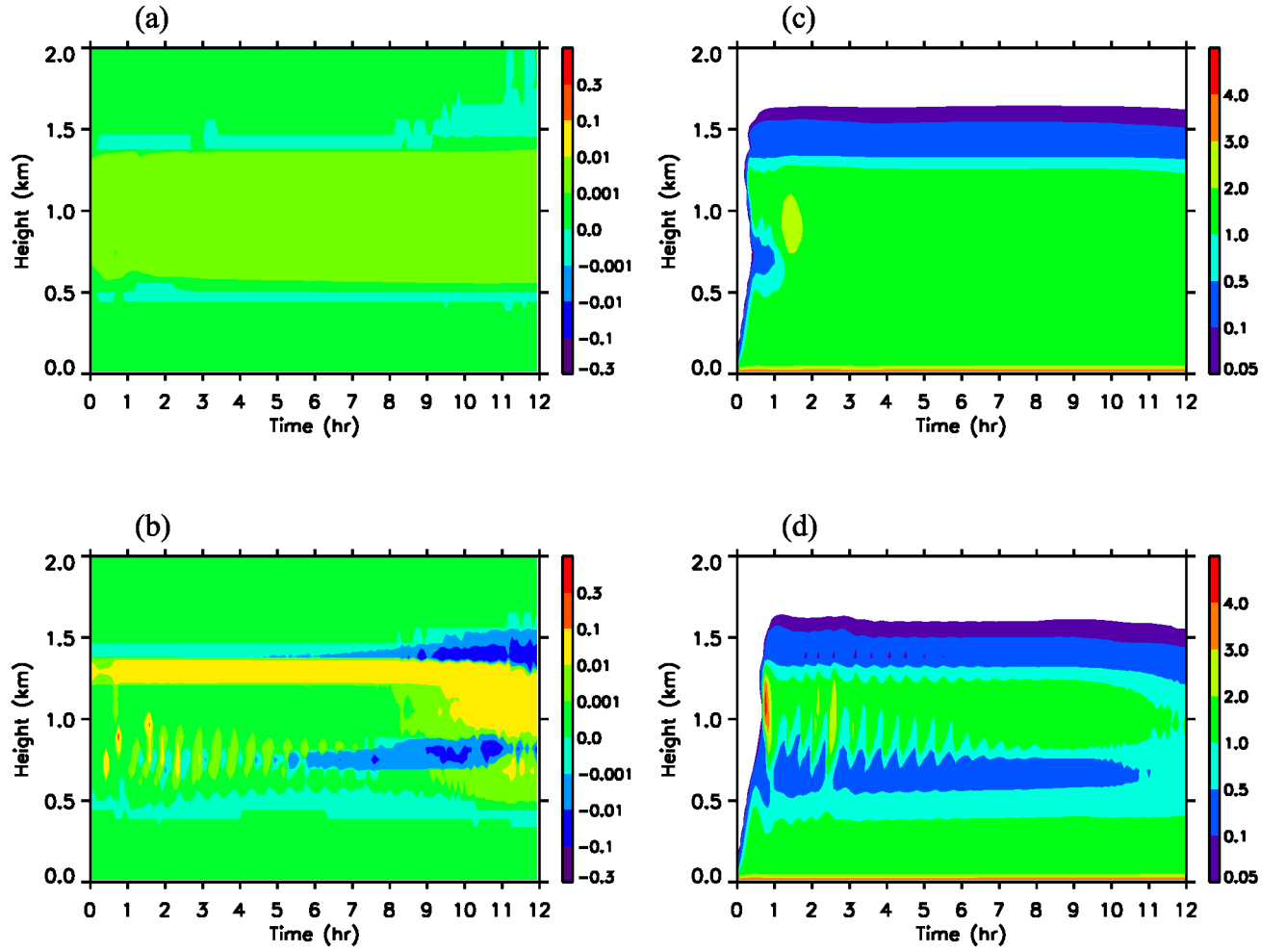


Figure 5. Time-height distribution of ice deposition rate ($\text{g kg}^{-1} \text{hr}^{-1}$) sampled at 5-min interval from the CONTROL (a) and OneM (b) simulations, respectively. Panels (c) and (d) are the same as (a) and (b) except for sub-grid turbulent kinetic energy ($\text{m}^2 \text{s}^{-2}$).

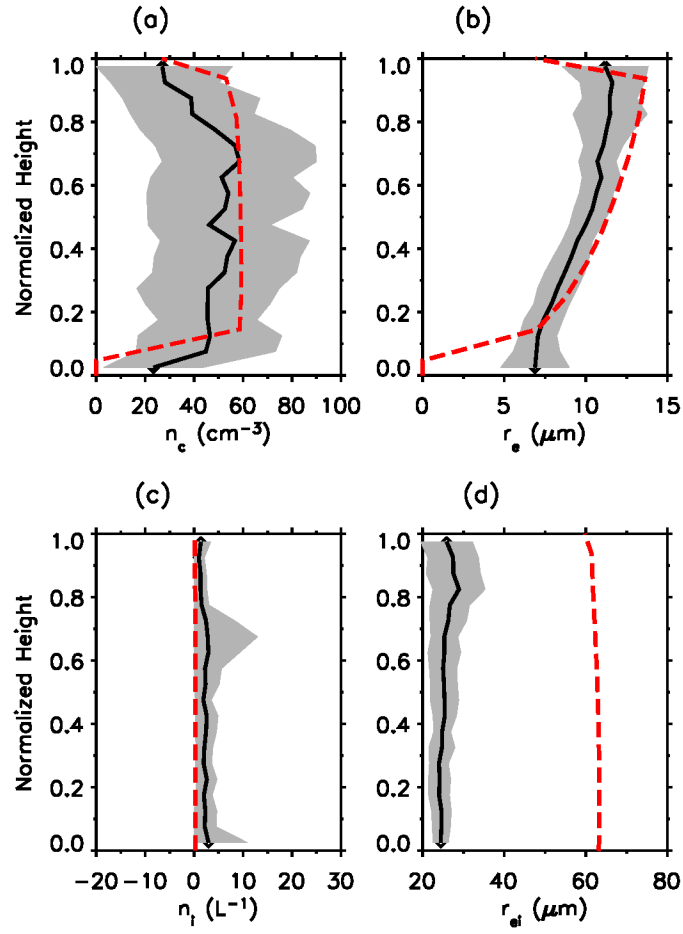


Figure 6. Vertical profiles of droplet number concentration (a), droplet effective radius (b), ice crystal number concentration (c), and ice crystal effective radius (d) from the CONTROL simulation (dashed lines) and the aircraft observations (solid lines representing the means and the shadows representing plus and minus one standard deviation).

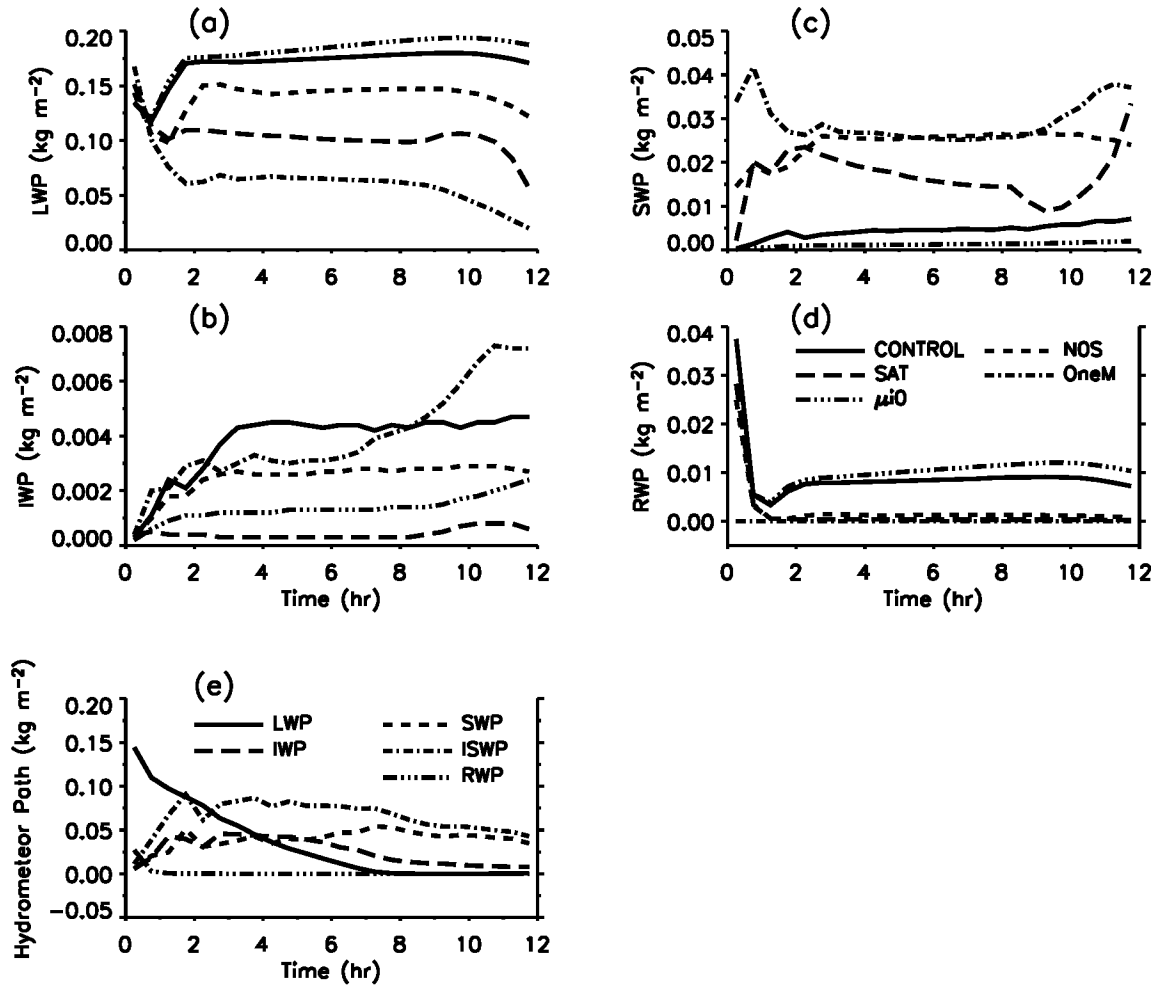


Figure 7. Time series of LWP (a), IWP (b), SWP (c), and RWP (d) produced by CRM simulations: CONTROL (solid), N0S (dots-dashed), $\mu i0$ (dotted), SAT (dot-dashed), and OneM (long-dashed with diamonds). Panel (e) represents time series of LWP (solid line), IWP (long dashed line), SWP (short dashed line), IWC plus SWP (dot-dashed line) and RWP (dots-dashed line) produce by the IN20 experiment.

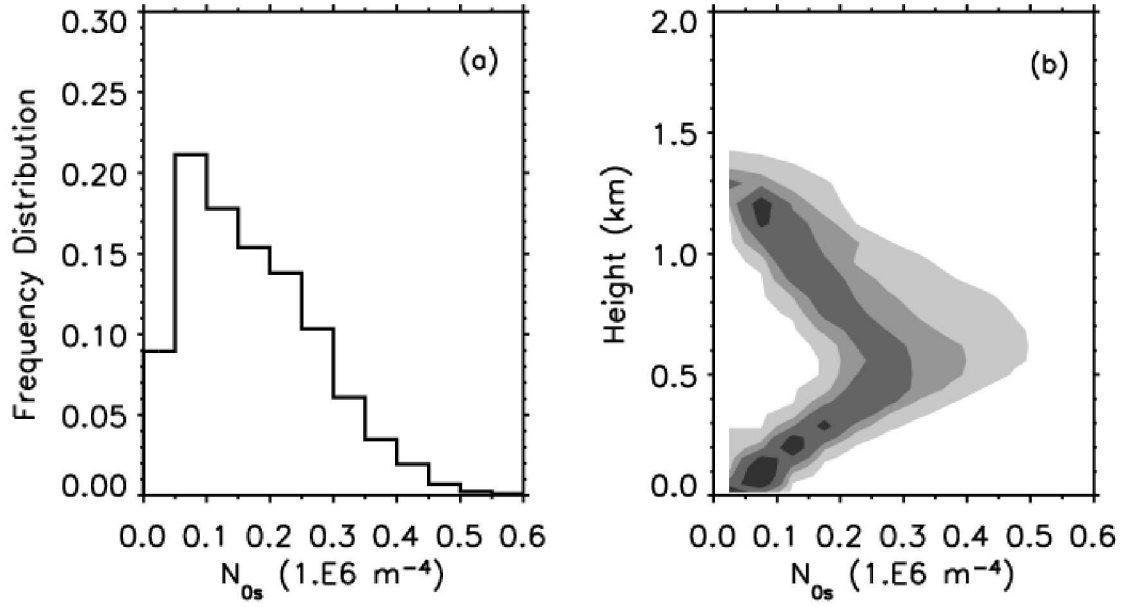


Figure 8. (a) Frequency distribution of N_{0s} predicted by the CONTROL simulation. (b) Joint PDF (%) of N_{0s} and height predicted by the CONTROL simulation. The contours from light to dark represent 0.1%, 0.5%, 1.0%, and 2.0%.

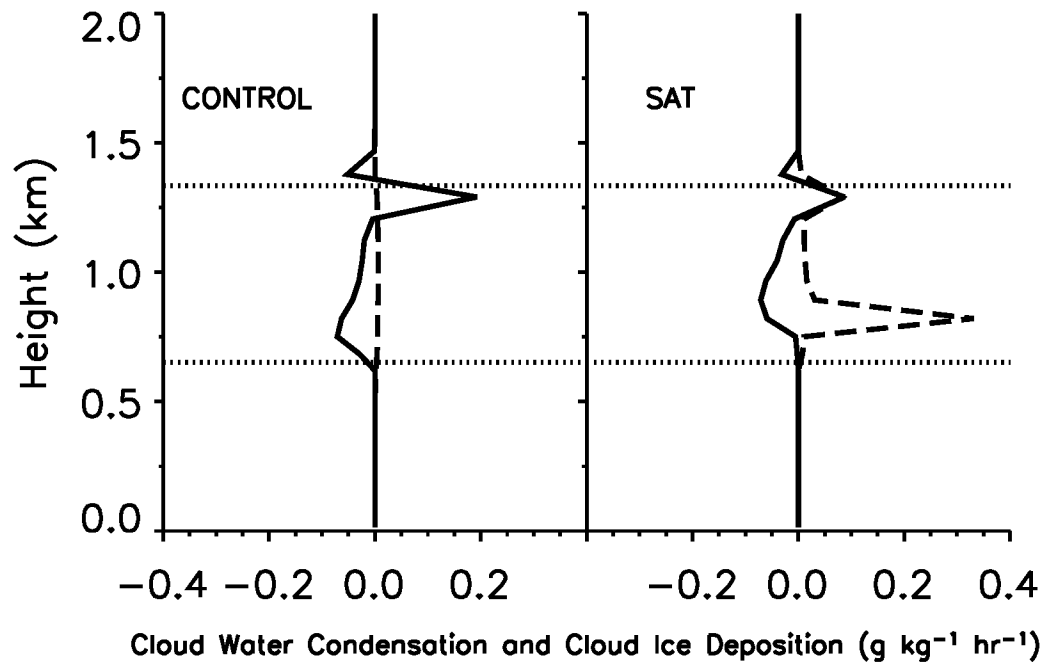


Figure 9. Vertical profiles of cloud water condensation (solid lines) and cloud ice deposition (dashed lines) averaged over the 12-hr period of the CONTROL (left) and SAT (right) simulations, respectively.

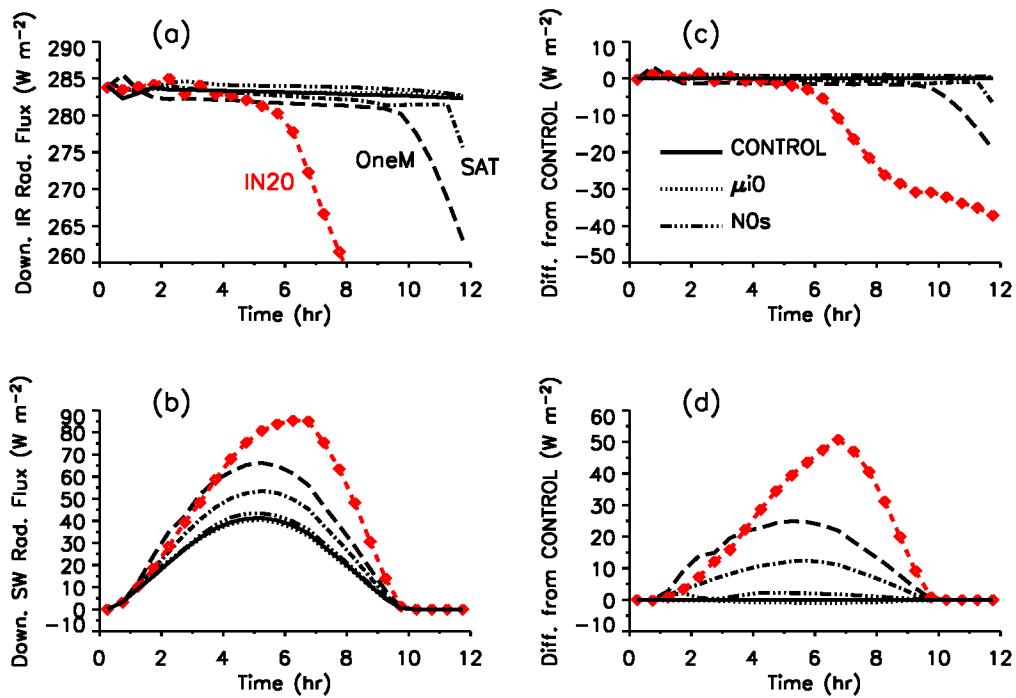


Figure 10. Time-series of half-hourly and horizontally averaged downwelling infrared (a) and shortwave (b) radiative fluxes at the surface in the CRM simulations. Panels (c) and (d) represent the differences in the infrared and shortwave fluxes, respectively, between the simulations and the CONTROL.

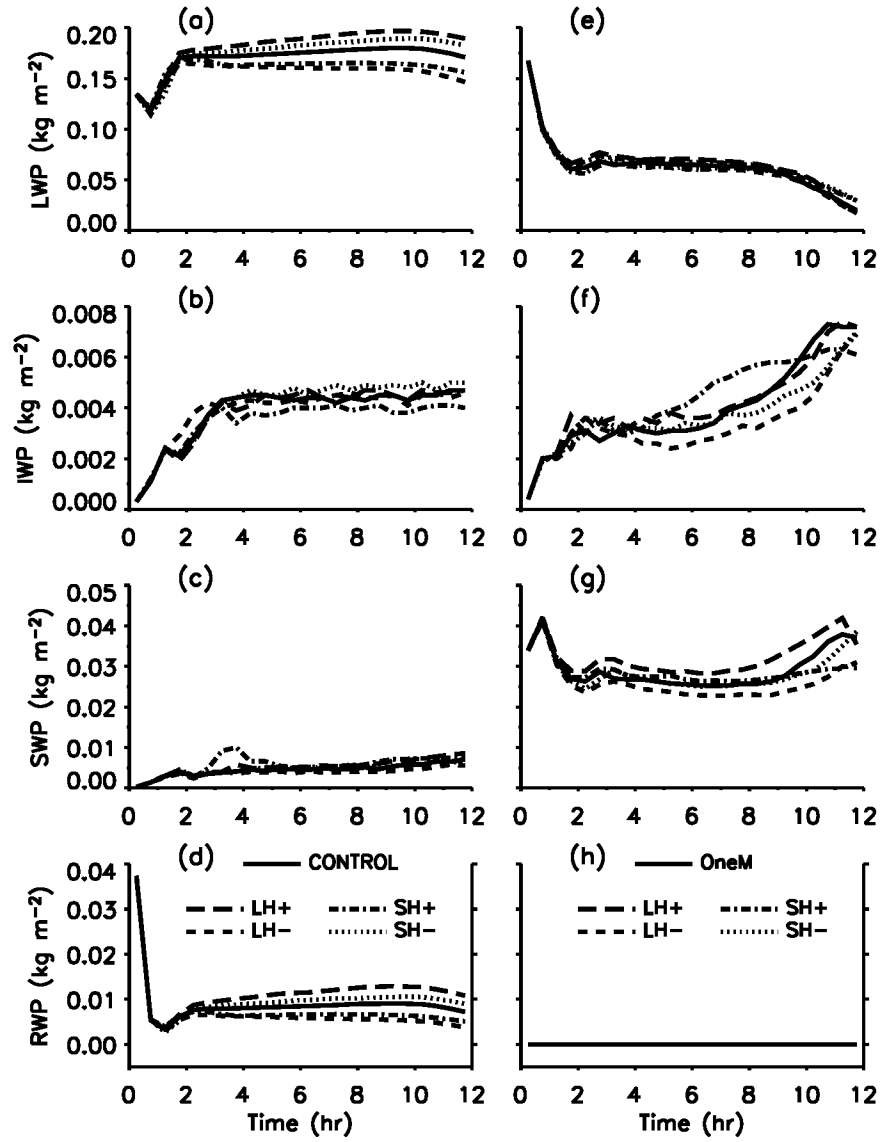


Figure 11. Time-series of half-hourly and horizontally averaged LWP (a, e), IWP (b, f), SWP (c, d), and RWP (d, h) from the experiments with the surface latent heat flux increased (long dashed lines) or decreased (short dashed lines) by 10%, or with the surface sensible heat flux increased (dot-dashed lines) or decreased (dotted lines) by 10%, respectively. Left panels: with the M05 scheme. Right panels: with the L83 scheme. The solid lines represent results from the CONTROL (left panels) and OneM (right panels) simulations.